CONTROLLING PRODUCT SELECTION AND REACTION MECHANISM OF PHOTOCATALYTIC REFORMING OF METHANOL INTO H_2 AND VALUABLE CHEMICALS USING COP CO-CATALYST

CHATIYA ARDCHON

A THESIS SUBMITTED IN PARTIAL FULFILLMENT
OF THE REQUIREMENT FOR THE DEGREE OF
MASTER OF ENGINEERING IN CHEMICAL ENGINEERING
SCHOOL OF ENGINEERING
KING MONGKUT'S INSTITUTE OF TECHNOLOGY LADKRABANG
2024

KMITL-2024-EN-M-227-308

การควบคุมการคัดเลือกผลิตภัณฑ์และกลไกปฏิกิริยาปฏิรูปเชิงแสงของเมทานอลสำหรับการผลิตเชื้อเพลิงไฮโดรเจนและสารเคมีที่มีมูลค่าด้วยตัวเร่งปฏิกิริยาเสริมโคบอลต์ฟอสไฟด์

CONTROLLING PRODUCT SELECTION AND REACTION MECHANISM OF PHOTOCATALYTIC REFORMING OF METHANOL INTO H_2 AND VALUABLE CHEMICALS USING COP CO-CATALYST

นายชาติยะ อาจชน

CHATIYA ARDCHON

วิทยานิพนธ์นี้เป็นส่วนหนึ่งของการศึกษาตามหลักสูตรปริญญาวิศวกรรมศาสตรมหาบัณฑิต

สาขาวิชาวิศวกรรมเคมี

คณะวิศวกรรมศาสตร์

สถาบันเทคโนโลยีพระจอมเกล้าเจ้าคุณทหารลาดกระบัง

พ.ศ. 2567

KMITL-2024-EN-M-227-308

หัวข้อวิทยานิพนธ์	การควบคุมการคัดเลือกผลิตภัณฑ์และกลไกปฏิกิริยาปฏิรูปเชิงแสงของเมทานอลสำหรับการผลิตเชื้อเพลิงไฮโดรเจนและสารเคมีที่มีมูลค่าด้วยตัวเร่งปฏิกิริยาเสริมโคบอลต์ฟอสไฟด์
นักศึกษา	นายชาติยะ อาจชน
รหัสประจำตัว	65016026
ปริญญา	วิศวกรรมศาสตรมหาบัณฑิต
สาขาวิชา	วิศวกรรมเคมี
พ.ศ.	2567
อาจารย์ที่ปรึกษาวิทยานิพนธ์	ผศ.ดร.ภัทรานิษฐ์ วงศ์พร้อมรัตน์

บทคัดย่อ

ไฮโดรเจนเป็นพลังงานหมุนเวียนที่สะอาดและมีศักยภาพอย่างมากสำหรับการใช้ทดแทนพลังงานจากเชื้อเพลิงฟอสซิลแบบดั้งเดิมที่ส่งผลกระทบต่อการเปลี่ยนแปลงสภาพอากาศ สิ่งแวดล้อม และเศรษฐกิจ กระบวนการผลิตไฮโดรเจนจึงเป็นหนึ่งในหัวข้อสำคัญที่ถูกศึกษาวิจัยกันอย่างแพร่หลายในเวลานี้ ในการศึกษานี้นำเสนอการสังเคราะห์ตัวเร่งปฏิกิริยาเชิงแสงโพแทสเซียม โพลี (เฮปตาซีนอิไมด์) (Potassium Poly(heptazine imide; K-PHI) เสริมด้วยตัวเร่งปฏิกิริยาร่วมโคบอลต์ฟอสไฟด์ (Cobalt phosphide; CoP) และแพลทินัม (Pt) เพื่อพัฒนากระบวนการผลิตไฮโดรเจนและผสมผสานกับการปฏิรูปของเมทานอล (Methanol reforming) เพื่อเป็นแนวทางใหม่ในการต่อยอดไปสู่การผลิตสารเคมีที่มีมูลค่าภายใต้การฉายแสงอาทิตย์ นอกจากนี้ยังตรวจสอบการก่อตัวของอนุมูลอิสระที่เกิดขึ้นระหว่างปฏิกิริยาและอธิบายบทบาทของอนุมูลอิสระเหล่านี้ต่อเส้นทางของปฏิกิริยา (Path of reaction) และการคัดเลือกผลิตภัณฑ์ผ่านการวิเคราะห์อิเล็กตรอนพาราแมกเนติกเรโซแนนซ์ จากการศึกษาพบว่าการเสริมตัวเร่งปฏิกิริยาร่วมช่วยปรับปรุงความสามารถในการคัดแยกประจุเชิงแสงและอัตราการเกิดปฏิกิริยาเป็นอย่างมากด้วยบทบาทที่แตกต่างกัน โคบอลต์ฟอสไฟด์จะทำหน้าที่เป็นตำแหน่งที่มีประสิทธิภาพ (Active site) ในการดักจับโฮลที่เกิดขึ้นจากการฉายแสงซึ่งช่วยส่งเสริมการเกิดอนุมูลไฮดรอกซิล (•OH) สำหรับการเปิดพันธะคาร์บอน-ไฮโดรเจนของเมทานอลและช่วยให้เกิดการควบคู่ (C-C Coupling) พันธะคาร์บอนของอนุมูลไฮดรอกซีเมทิล ($\bullet CH_2OH$) สำหรับการผลิตเอทิลีนไกลคอล ในทางกลับกัน แพลทินัมนั้นมีประสิทธิภาพในการดักจับ

อิเล็กตรอนเพื่อเพิ่มอัตราการผลิตไฮโดรเจนผ่านการควบคู่ (H-H Coupling) ของอนุมูลไฮโดรเจน (•H) และส่งเสริมการผลิตอะซิเตทผ่านการสร้างอนุมูลเมทิล ($•CH_3$) และอนุมูลคาร์บอนไดออกไซด์ประจุลบ ($•CO_2^-$) ซึ่งมาจากปฏิกิริยาการดึงน้ำออกจากเมทานอล โดยตัวเร่งปฏิกิริยาร่วมทั้งสองชนิดแสดงค่าการเลือกจำเพาะ (Selectivity) ของผลิตภัณฑ์ใกล้เคียง 100% ทั้งในเฟสแก๊สและของเหลว งานวิจัยนี้แสดงให้เห็นถึงบทบาทที่สำคัญของตัวเร่งปฏิกิริยาร่วมในการควบคุมเส้นทางของปฏิกิริยาและการคัดเลือกผลิตภัณฑ์ โดยให้ข้อมูลเชิงลึกที่สำคัญที่สามารถนำไปใช้ในการปรับปรุงกระบวนการเชิงแสงด้วยตัวเร่งปฏิกิริยาเพื่อการผลิตเชื้อเพลิงจากแสงอาทิตย์และการสังเคราะห์สารเคมีอย่างยั่งยืน

คำสำคัญ ตัวเร่งปฏิกิริยาร่วมโคบอลต์ฟอสไฟด์ ตัวเร่งปฏิกิริยาร่วมแพลทินัม การผลิตไฮโดรเจน การปฏิรูปเมทานอล

Thesis title	Controlling Product Selection and Reaction Mechanism of Photocatalytic Reforming of Methanol into H_2 and Valuable Chemicals Using CoP co-catalyst
Student name	Mr. Chatiya Ardchon
Student ID.	65016026
Degree	Master of Engineering
Program	Chemical Engineering
Year	2024
Advisor	Asst. Prof. Dr. Patthranit Wongpromrat

ABSTRACT

Hydrogen is regarded as a clean and sustainable energy with significant potential to replace the traditional fossil fuels. Photocatalytic H_2 production combined with reforming of methanol by using photocatalysts under solar irradiation offers a novel approach to generate valuable chemicals while addressing environmental and economic challenges. In this study, photocatalyst potassium poly(heptazine imide) (K-PHI) deposited with CoP co-catalyst and Pt co-catalyst were synthesized for simultaneous production of H_2 and valuable chemicals from photocatalytic reforming of the methanol solution under solar irradiation. Electron paramagnetic resonance analysis was used to investigate the formation of intermediate free radicals and elucidate their roles in influencing reaction pathways and product selection. The presence of co-catalysts substantially improved the separation of the photogenerated charges and therefore the reaction rates with the distinct roles. CoP served as an efficient site for hole trapping, promoting the formation of reactive •OH radicals to activate the C-H bonds in methanol and enabling effective C-C coupling of $•CH_2OH$ to produce

ethylene glycol. In contrast, Pt site efficiently trapped electrons to enhance the H_2 production through the coupling of •H radicals and facilitated the formation of acetate via the generation of $•CH_3$ and $•CO_2^-$ radicals, derived from photocatalytic dehydration of methanol. The selectivity of the products is close to 100% in the gas and liquid phases. This work demonstrates the pivotal roles of co-catalysts in controlling reaction pathways and product selection, offering significant insights into optimizing further photocatalytic processes for solar fuel production and sustainable chemical synthesis.

Keywords: Carbon nitride photocatalyst, Cobalt phosphide co-catalyst, Platinum co-catalyst, H_2 production, Methanol reforming

ACKNOWLEDGEMENT

I would like to thank my advisor, Professor Hsisheng Teng for his guidance and support throughout my research journey and master's degree study. His advice and mentorship have been instrumental in overcoming numerous problems and provided guidelines for completing this research, including various teachings that allowed me to develop myself and become a person with quality in both professionalism and attitude. There was also help in many other matters that made my experience abroad smooth and happy.

Additionally, I am deeply grateful to My advisor from Thailand, Assistant Professor Patthranit Wongpromrat for providing me with the opportunity to study in Taiwan and being the starting point for me to see my flaws and pushing me to be a better person in every way, also advice and lots of help as well.

Moreover, I would like to thank members of the Water Splitting group, Can and Lisa, for their discussion of solving problems and improving my research, as well as for teaching me how to work with various tools and instruments in detail. Also, Doris, Rias and the members of the Battery and Supercapacitor, Albert, Tony, Leon, Hahn, Steven, Bebe, Zev, Jean, Vivian, Johnny and David for their assistance with many works, coordination, important documentation and very good friendship which helped me settle in so quickly. Finally, I would like to express my gratitude to my family in Thailand for their love, support, and encouragement. Appreciate it sincerely.

Chatiya Ardchon

TABLE OF CONTENTS

Chapter **Page**

LIST OF FIGURES

Figure **Page**

LIST OF TABLES

Table **Page**

CHAPTER 1 INTRODUCTION

The environmental challenges associated with traditional fossil fuel consumption have intensified the need for alternative energy sources. Developing sustainable and economically viable approaches using renewable energy is crucial [1,2,3]. Hydrogen is regarded as a clean and sustainable energy and has a significant potential to replace conventional fossil fuels. The production of hydrogen through water decomposition using photocatalysts under solar irradiation has gained considerable attention as an effective solution to environmental and economic issues [4,5]. When this reaction was combined with methanol photoreforming in aqueous systems, it represents an innovative approach. This combination process not only produces various valuable chemicals but also addresses environmental concerns while advancing green chemistry technologies. The selection of photocatalysts with co-catalysts for optimizing the reaction pathways and product selection remains a significant challenge [6].

Various photocatalysts have been utilized for light-absorbing conversion, including TiO_2, ZnO, CdS, and C_3N_4. However, these materials typically suffer from low photocatalytic performance due to limited solar light absorption, inefficient charge separation and migration [7,8,9]. To address these limitations, potassium poly(heptazine imide) (K-PHI), derived from polymeric carbon nitride (PCN), has emerged as a promising photocatalyst. K-PHI exhibits exceptional photocatalytic activity owing to its superior optical and electronic properties. Notable advantages of K-PHI include its low cost, ease of synthesis, strong light absorbance and suitable

electronic redox levels. Additionally, K-PHI is capable of stabilizing photogenerated charge carriers and favorable structural attributes, such as optimal crystallite size and minimal defects, enhancing its potential as a photocatalyst for advanced photocatalytic applications [10].

However, enhancing photocatalytic activity is often hindered by the fast internal recombination of photogenerated carriers and inefficient surface charge utilization within the photocatalyst. According to the literature, integrating a co-catalyst is effective in overcoming these limitations by improving the separation of photogenerated electron–hole pairs and providing active sites for interfacial reactions. Noble metals such as Pt are the effective co-catalysts for hydrogen production because they capture and transfer photogenerated electrons, leaving photoholes in the photocatalyst's valence band [11,12]. On the other hand, transition metal phosphides (TMPs), including CoP, FeP, MoP, and Ni_2P, have gained significant attention as an alternative co-catalyst for photocatalytic reactions due to their cost-effectiveness, noble metal-free, high electrical conductivity, and suitability for large-scale applications. Among these TMPs, CoP has emerged as a particularly promising co-catalyst, offering an excellent catalytic activity and stability in both reductive and oxidative processes [13,14].

In photocatalytic methanol reforming under basic conditions, H_2O reduction generates •H radicals and OH^- by consuming photogenerated electrons, with the •H radicals subsequently coupling to produce H_2 [15]. On the oxidation side, the formation of multi-carbon (C_2+) products via C-C coupling is preferred due to their higher

economic value compared to C_1 products [16,17]. The reforming reaction can produce a wide range of products, depending on the activity of photogenerated charges that influence the intermediate radical formation, leading to various reaction pathways. Therefore, the functional role of co-catalysts is pivotal in guiding this complex C-C coupling process and controlling the photoreforming reactions [18,19,20]. A deep understanding of co-catalysts properties and their roles in photocatalytic reactions is crucial for advancing the field of photocatalysis, investigating the diverse effects of co-catalysts can elucidate the charge transfer mechanisms and the interplay between reductive H_2 evolution and oxidative methanol reforming into valuable chemicals.

In this study, we report the synthesis of the K-PHI and investigate the functional roles of CoP compared with Pt co-catalysts in influencing product selection and reaction mechanisms for the simultaneous production of H_2 and valuable chemicals through photocatalytic methanol reforming under solar irradiation. The presence of these co-catalysts significantly improves the separation and migration of photogenerated charges, resulting in effective performance for both H_2 production and methanol reforming. Through the identification and analysis of intermediate free radicals, the distinct roles of CoP and Pt were observed. These results highlight the potential of co-catalyst modification to fine-tune reaction pathways, offering promising advancements in solar fuel production and sustainable chemical processes.

CHAPTER 2 EXPERIMENTAL SECTION

2.1 Materials Synthesis

2.1.1 K-PHI Photocatalysts

A 20 g of melamine (99%, Sigma-Aldrich, USA) was calcined in a crucible with a lid at 550 °C for 4 h using a 2 °C min^{-1} of ramp rate, followed by natural cooling to room temperature. The polymeric carbon nitride (PCN) was obtained by grinding the calcined material into a powder.

K-PHI was prepared by grinding 1 g of PCN mixed with 2 g of KSCN (99%, Sigma-Aldrich, USA). The mixture was loaded into an alumina boat and placed in a tube furnace. The powders were heated to 400 °C with a 25 °C min^{-1} of ramp rate in an argon atmosphere and held at 400 °C for 60 min. Subsequently, the temperature was increased to 500 °C at a 25 °C min^{-1} of ramp rate and held at this temperature for 30 min. After naturally cooling down, the obtained K-PHI catalyst powders were washed and dried overnight in a vacuum oven at 60 °C [10].

2.1.2 CoP@K-PHI Photocatalysts

A 1.2 g of $Co(NO_3)_2 \cdot 6H_2O$ (≥98%, Alfa Aesar, England) was dissolved in 100 mL of deionized water with stirring. A 16 mL of 0.5 M NaOH solution was subsequently dropped into the solution and continuously stirred for 4 h at room temperature. The obtained $Co(OH)_2$ was washed and dried under vacuum at 60 °C overnight. Then, 50 g of $Co(OH)_2$ and 500 mg of $NaH_2PO_2 \cdot H_2O$ were positioned on

the both sides of the alumina boat, with $Co(OH)_2$ placed at the downstream side in the tube furnace. The samples were heated at 430 °C with a 2 °C min^{-1} of ramp rate and kept for 1 h in the continuous argon atmosphere to get CoP co-catalyst. Afterward, the CoP co-catalyst was washed with diluted HCl solution followed by deionized water and then dried at 60 °C for 6 h.

After attaining both K-PHI and CoP, a 50 mg of K-PHI was ground with 5 wt% of CoP resulting a CoP@K-PHI which was subsequently calcined at 300 °C for 1 h under an argon atmosphere in the tube furnace to enhance the interfacial interactions [21].

2.2 Photocatalytic Reforming of Methanol

In a Pyrex reaction vessel with side-irradiation (4 cm in diameter of flat illumination window) connected to a closed glass gas circulation system and using a solar simulator (Oriel Instruments, AM 1.5 G, 100 mW cm^{-2}, USA) as the irradiation source, all photocatalytic reactions were conducted. Before irradiation, the reaction system was degassed to remove air and lowered the system pressure to 0.1 bar. Subsequently, 50 mg of CoP@K-PHI was suspended and sonicated in a 250 mL solution containing 225 mL of deionized water and 25 mL of methanol (≥99.9%, Aencore, Australia). and the pH of this solution was adjusted to be 9 by using 0.5 M NaOH. The reaction system was carried out over 4 days, with gas product analyzed by gas chromatography (GC, GC-2014, Shimadzu, Japan) using a thermal conductivity detector and Ar as the carrier gas. The reaction system was operated and evacuated

every 12 h. Liquid product was analyzed by gas chromatography-mass spectroscopy (GC-MS, QP2010, Shimadzu, Japan) every 12 h and stored at 4 °C.

For comparison, CoP@K-PHI was substituted with K-PHI and 3-wt% $H_2PtCl_6 \cdot 6H_2O$ was in-situ deposited into the solution as a co-catalyst, then analyzed and compared with the conditions described above.

2.3 Characterization of Photocatalysts

2.3.1 High-Resolution Transmission Electron Microscopy (HR-TEM)

High-resolution transmission electron microscopy (HR-TEM) is a powerful analytical technique used to image the internal structure of materials at the atomic scale. Unlike conventional transmission electron microscopy (TEM), which offers imaging resolutions typically on the order of nanometers, HR-TEM achieves sub-angstrom resolution, enabling researchers to visualize individual atoms and atomic columns within crystalline materials. It is an effective method for obtaining additional data, such as crystal lattice, defects, grain boundaries and interfacial analysis.

The principle of HR-TEM lies in its ability to utilize phase contrast imaging, which is generated by the interference of electron waves scattered by the specimen. As an electron beam passes through a thin sample, it interacts with the atomic potentials of the material, causing the beam to diffract. The transmitted and diffracted beams interfere with each other, forming a complex wavefront. When this wavefront is projected onto an imaging device, it produces an interference pattern that corresponds to the atomic structure of the specimen achieving optimal resolution [22,23,24]. The

transmission electron microscopy **(**Jeol 2100 F, Japan**)** was used to perform HR-TEM for the data of the catalysts in this study.

2.3.2 X-ray Diffraction (XRD)

X-ray Diffraction (XRD) is an analytical technique used to determine the purity and structure of crystalline materials. This method works by irradiating the target materials with a monochromatic X-ray beam, which interacts with the crystal planes and produces diffraction patterns through constructive and destructive interference. These diffraction patterns provide critical information about the long-range order of crystalline solids and are used to identify specific crystalline materials due to their unique atomic structures. XRD is typically used as a fundamental characterization tool for the structural and compositional analysis of materials. Through XRD analysis, researchers can gain valuable insights into the crystallographic phase, lattice parameters, and overall purity of these materials, which are essential for developing and optimizing various catalytic processes [25].

In this study, XRD analysis was performed using a Rigaku X-ray diffractometer (Rigaku RINT-2000, Japan) equipped with a Cu-Kα radiation source. The measurements were conducted with a count rate of 10 seconds per 0.05° increment over a 2θ range of 10–80° for catalyst analysis.

2.3.3 In-Situ Fourier Transform Infrared Spectroscopy (FTIR)

Fourier Transform Infrared (FTIR) Spectroscopy is a powerful analytical technique used to investigate the interaction between infrared (IR) radiation and a sample, which can be in solid, liquid and gaseous forms. This technique measures both the frequencies and intensities at which the samples absorb IR radiation, enabling the identification of the samples' chemical composition. The specific absorption frequencies correspond to the chemical functional groups absorbing radiation at unique frequencies. The intensities of these absorptions can also be used to determine the concentrations of specific components within the sample. The resulting IR spectrum is a two-dimensional plot of intensity versus frequency, serving as a fingerprint for identifying chemical compounds. FTIR spectroscopy is applicable to a wide range of materials and conditions, making it an invaluable tool for both qualitative and quantitative analyses of functional groups and molecular bonds [26]. In this study, the catalyst powders were embedded in potassium bromide (KBr) pellets before analyzing FTIR spectra using Nicolet 6700 spectrometer (Thermo Fisher Scientific Inc., USA).

Fourier transform spectrophotometer provides rapid and detailed spectral analysis by emits a beam of IR radiation from a glowing black-body source, which passes through an interferometer where spectral encoding occurs. In the interferometer, beams with different path lengths combine to create interference patterns known as interferograms. These beams then enter the sample compartment, where specific frequencies are absorbed by the sample leading to produce a characteristic absorption pattern. A detector records the interferogram signal, measuring energy versus time across all frequencies simultaneously. A reference beam is superimposed to ensure

accurate measurements. The final spectrum is obtained by using Fourier transformation software to subtract the background spectrum, yielding a precise representation of the sample's absorption characteristics. This advanced capability makes FTIR spectroscopy an essential technique in the analysis and identification of complex chemical structures [27].

2.3.4 X-ray Photoelectron Spectroscopy (XPS)

X-ray Photoelectron Spectroscopy (XPS), also known as Electron Spectroscopy for Chemical Analysis (ESCA), is a technique used to measure the core-level binding energies (BEs) of photoelectrons ejected from atoms at/near the surface of the sample. By analyzing the peak heights, relative binding energies and peak areas, XPS can identify the elemental composition and estimate their relative concentrations on the surface along with the expected bonding of the materials. This surface-sensitive spectroscopic method provides detailed information about the elemental composition, chemical state, and electronic structure of the materials, which is crucial for understanding their properties and potential applications. XPS is particularly effective in revealing both the presence of specific elements and their interactions with other elements. Moreover, XPS also provides insights into the chemical and electronic states of core-ionized atoms through the analysis of BE shifts and satellite structures. Proper interpretation of BE shifts is critical for obtaining material information necessary to predict catalytic properties and understand surface chemistry. XPS is frequently used for depth profiling when combined with ion-beam etching and for line profiling of

elemental compositions across surfaces [28]. The XPS (AXIS Ultra DLD, Kratos, UK) equipped with an Al-Kα radiation source was used to analyze the chemical structure and composition of the prepared catalysts in this study.

2.4 Optical and Photophysical Properties of Photocatalysts

2.4.1 UV-Visible Spectroscopy (UV-Vis)

UV-Visible spectroscopy is a rapid analytical technique that measures the absorbance or transmittance of light at specific wavelengths to understand electronic transitions in molecules. These transitions occur when light excites electrons from a lower energy orbital, known as the highest occupied molecular orbital (HOMO), to a higher energy unoccupied orbital, known as the lowest unoccupied molecular orbital (LUMO). Although the UV wavelength spans from 100 to 380 nm and the visible component extends up to 800 nm, the most spectrophotometers operate within a practical range of 200–1100 nm. This range covers UV, visible, and a part of the near-infrared spectrum, with the practical application of UV-Visible spectroscopy focused between 200 and 800 nm. Below the wavelength of 200 nm, it is known as vacuum UV while the wavelength above 800 nm extends into the infrared region.

Light interacts with samples in various ways: it can be transmitted through media, reflected surfaces, or refracted by crystals. The absorbance of light at specific wavelengths is attributed to covalently unsaturated compounds, known as chromophores, which are responsible for the colors observed in the materials. These compounds absorb UV-visible light due to electronic transition energy differences that

match the energy of the incident light. In addition to chromophores, auxochromes are groups that do not directly absorb UV-visible light but influence the absorption characteristics of chromophores. Auxochromes are electron-donating groups that enhance the color intensity of chromophores without altering their own color. When UV-visible radiation interacts with chromophores, it induces electron excitation, where electrons in the ground state transition to an excited state. This phenomenon is crucial for understanding the optical properties and behavior of materials. UV-visible spectrophotometers utilize a light source directed through a sample, with a detector on the opposite side to measure the transmitted light. The recorded transmittance data reveals how much light is absorbed at each wavelength, providing valuable insights into the molecular structure and composition of the sample. By analyzing the absorption spectra, researchers can identify functional groups, quantify concentrations, and assess the purity of various chemical compounds [29,30].

2.4.2 Photoluminescence (PL)

When a material absorbs light of sufficient energy, photons excite electrons to higher energy levels, creating electronic excitations. As these excitations relax, the electrons return to the ground state. Photoluminescence (PL) is the emission of light from a material as it transitions from an electronically excited state to the ground state, following the absorption of energy from an external light source. PL spectroscopy involves measuring parameters such as lifetime, intensity, and line shape, and has become a widely used non-contact and non-destructive technique for analyzing the

properties of photocatalysts and various materials [31]. With a fluorescence spectrophotometer **(**F-700, Hitachi, Japan**)**, steady state PL spectra of the prepared catalysts in this work were revealed.

The photoluminescence intensity can be further analyzed under varying external parameters, such as temperature and applied voltage, to gain deeper insights into the material's electronic states and bands. PL is inherently dependent on the nature of the optical excitation. The energy of the excitation determines the initial photoexcited state and affects the penetration depth of the incident light. The PL signal's intensity often correlates with the density of photoexcited electrons, allowing researchers to adjust the incident beam's intensity to control this parameter. This makes PL spectroscopy a versatile tool for investigating the optical and electronic properties of materials, helping researchers explore various phenomena such as energy band gaps, defect states, and charge carrier dynamics [32].

2.4.3 UV Photoelectron Spectroscopy (UPS)

Photoelectron Spectroscopy (PES) is an analytical technique that measure the excitation of a sample by photons to release photoelectrons, providing insights into the electronic structure of materials. When a material is illuminated with light of a specific wavelength, electrons are emitted if the light's energy is sufficient to overcome the sample's work function which is the minimum energy needed to dislodge an electron from the Fermi level to an external rest state. UV Photoelectron Spectroscopy (UPS)

focuses on the UV range, with the excitation energy between 8 and 50 eV. During UPS measurement, a sample is exposed to monochromatic UV light.

UPS is effective for examining surface electronic states, as it operates with high-resolution spectral excitation sources like He I and He II gases, ensuring excellent monochromaticity [33]. The primary function of UPS is to analyze the spin separation of ions, resonance structures, energy band structures, void states, or surface states of materials. Although UPS operates similarly to X-ray Photoelectron Spectroscopy (XPS), it utilizes lower energy than X-rays, which are typically employed for examining core-level electrons. X-rays can only effectively target outer valence electrons and those in the valence band, providing high energy resolution. Conversely, UPS offers superior resolution for investigating the electronic structure of the valence band due to its ability to assess the energy distribution of electrons within the valence shell. By analyzing the energy distribution of these electrons, UPS can extract relevant information such as valence band energy, work functions, and electron density distributions. This makes UPS a tool for understanding the material properties at the electronic level, aiding in the study of complex electronic configurations [34].

2.5 Gas Chromatography-Mass Spectrometry (GC-MS)

Gas Chromatography-Mass Spectrometry (GC-MS) is a widely used analytical platform for analyzing volatile and thermally stable chemicals, offering precise separation and identification capabilities. For the gas chromatography, samples are typically diluted or dissolved in a solvent and then injected into the heated intake port,

where they vaporize into a gaseous state. The sample is then carried through the column by an inert gas serving as the mobile phase. Different components within the sample interact variably with the stationary phase, causing them to move through the column at distinct rates. This differential movement leads to the separation of sample components detected as they exit the column. The resulting chromatogram shows peaks that represent each separated compound. The height of each peak indicates the quantity of the compound detected, while the position of the peak corresponds to the time it takes for the compound to move through the column.

After the separation in the GC, each compound is introduced to the mass spectrometer (MS) for further analysis. It is started with the ionization process occurring to break the compounds into charged particles or ions by directing a high-energy electron beam at the molecules of the sample. These ions are characterized by their mass-to-charge ratio (m/z), calculated by dividing the fragment's mass by their charges. The ions are then subjected to a magnetic field and accelerated through a tunnel, leading to their deflection based on m/z ratios. Upon reaching the detection plate, the relative abundance and m/z ratios are determined, resulting in the creation of a mass spectrum. This spectrum—a graphical representation of signal strength or abundance of each fragment versus its m/z ratio for each chemical compound. Although GC-MS excels in analyzing volatile and low to moderate molecular weight compounds, it is limited to mass range and lower effectiveness for high molecular weight molecules. Nevertheless, GC-MS remains a powerful tool in identifying complex mixtures due to its precise separation and detection capabilities [35].

The GC-MS analysis for the liquid products in this study (1 µL samples) was conducted by using a Shimadzu GC-2010 gas chromatograph (Japan) fitted with an HP-INNOWAX column (60 m x 0.25 µm x 0.32 mm; Agilent Technologies, USA), in conjunction with a Shimadzu GCMS-QP2010 mass spectrometer (Japan) using helium as the carrier gas. The analysis was performed under specific conditions: a pressure of 91.8 kPa, a total flow rate of 24.7 mL min^{-1}, a column flow rate of 2.2 mL min^{-1}, a linear velocity of 37.9 cm s^{-1}, a purge flow of 5 mL min^{-1}, a split ratio of 10, an oven temperature of 40°C, and an injection temperature of 150°C. Within the GC oven, the temperature program was set to be 40°C for 15 minutes, followed by an increase of 25°C min^{-1} to 200°C, maintained for 20 minutes. The mass spectrometry settings were as follow: an ionization energy of 70 eV, an ion source temperature of 230°C with electron ionization mode, an interface temperature of 250°C, a solvent cut time of 1 minute, a detector gain of 0.8 kV, thresholds of 5, a start time of 2 minutes, an end time of 5.58 minutes, acquisition mode for selected ion monitoring, and a mass range of 0 to 100 m/z. Data analysis was carried out using Shimadzu's GC-MS Solution Software, version 4.30.

2.6 Electron Paramagnetic Resonance Spectroscopy (EPR)

Electron Paramagnetic Resonance (EPR) is a form of spectroscopy that is used to examine intermediates or radicals in reactions through their interaction with electromagnetic waves. It is crucial for understanding the reactivity of the sample chemical species. Unlike most spectroscopies where the energy is varied, EPR typically

maintains a constant frequency while sweeping the magnetic field. This approach changes the energy levels of the sample to match the spectrometer, allowing for precise analysis. The resonance condition is achieved by applying an external magnetic field, which separates the degenerate spin energy levels to align with the energy of microwaves. Paramagnetic materials, which become magnetized in the presence of a magnetic field without retaining a permanent magnetic moment, possess the necessary electron spin energy levels for this analysis. The magnetic dipole moment of unpaired electrons serves as the physical basis for this paramagnetism, making EPR an invaluable tool in exploring the electronic structure and dynamics of paramagnetic substances [25].

EPR analysis for this study was performed by using Miniscope MS-5000 EPR spectrometer (Freiberg Instruments, Germany), equipped with a 0.575-W visible-light laser (462 nm single wavelength) and high-power light-emitting diode as the light source for spectrometer. 5,5-Dimethyl-1-Pyrroline-N-Oxide (DMPO) was added to detect radicals in the 50 μL sample solution. All samples were exposed to radiation for 1 min. The measurement parameters included a field modulation of 0.2 mT, modulation frequency of 100 kHz, scan range of 15 mT, and microwave power of 10 mW.

CHAPTER 3 RESULTS AND DISCUSSION

3.1 Preparation and Characterization of Photocatalysts

To characterize the microstructures of K-PHI and CoP@K-PHI, the TEM and HR-TEM analyses were performed. In Figure 1a, CoP can be clearly observed in the black area, which was evenly distributed on K-PHI in the gray area. HR-TEM image in Figure 1b further reveals distinct characteristics of CoP. The lattice spacings of 0.199 nm and 0.245 nm corresponded to the (211) and (102) planes of CoP, respectively [36,37]. Moreover, EDS elemental mapping results of CoP@K-PHI in Figures 1c and d show that Co and P elements in CoP were distributed on K-PHI.

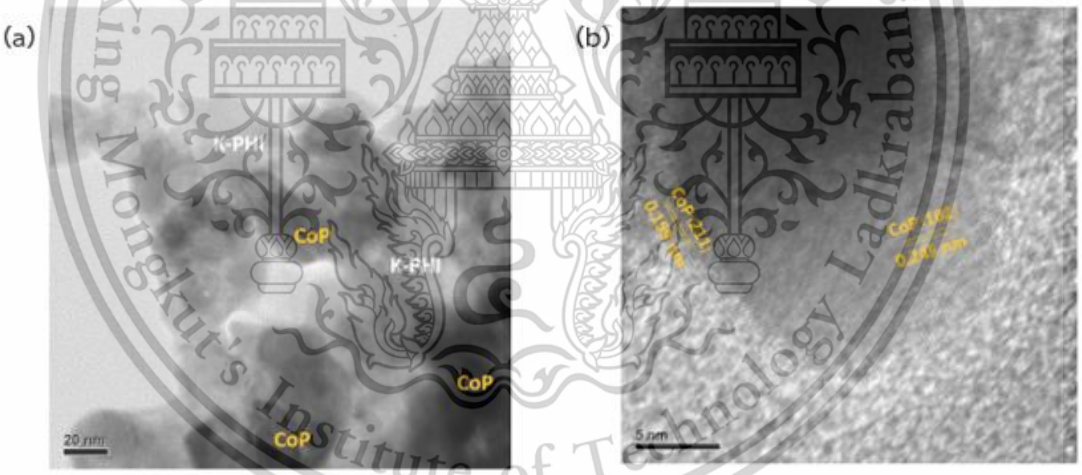

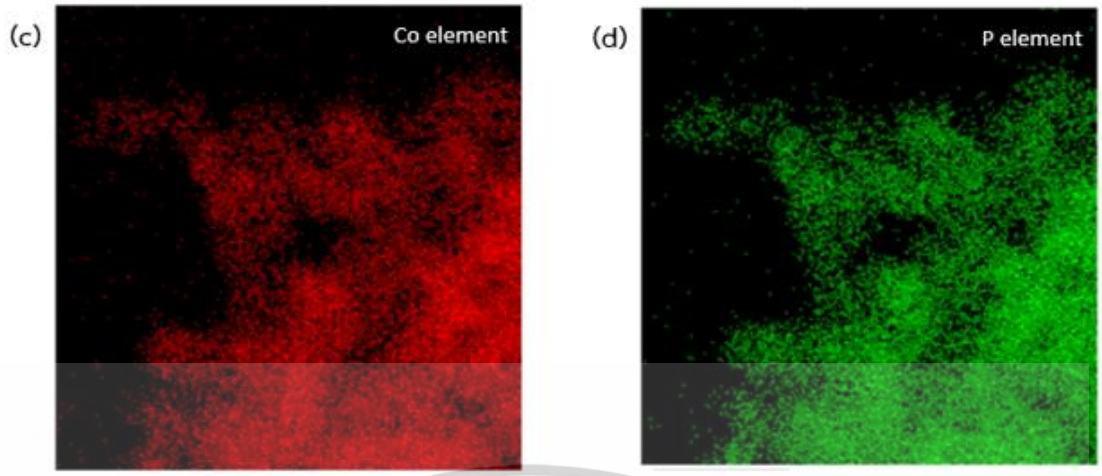

Figure 1 (a) TEM image (b) HR-TEM image and (c-d) EDS elemental mappings of CoP@K-PHI.

Figure 2 illustrates the XRD patterns of CoP, K-PHI, and CoP@K-PHI. K-PHI exhibited two weak diffraction peaks at 8° and 9.67° along with the main peak at 28.16°, related to the ($\bar{1}$10), (010), and (002) planes of K-PHI, respectively [38,39]. For pure CoP, the diffraction peaks located at 31.63° and 36.5° corresponded to the (011) and (102) planes [40], while the peaks at 46.28°, 48.18° and 56.72° can be indexed to the (112), (211) and (013) planes of CoP, respectively [41]. The XRD pattern of CoP@K-PHI still exhibits the characteristic diffraction peaks of both CoP and K-PHI with no obvious shift observed. These observations indicate that the introduction of CoP co-catalyst did not affect the crystal structure of K-PHI catalyst. Moreover, the peaks with low intensities of the CoP in CoP@K-PHI samples might be attributed to its low content

and high dispersion. Figures 1 and 2 demonstrate the successful preparation and integration of CoP co-catalyst into K-PHI catalyst.

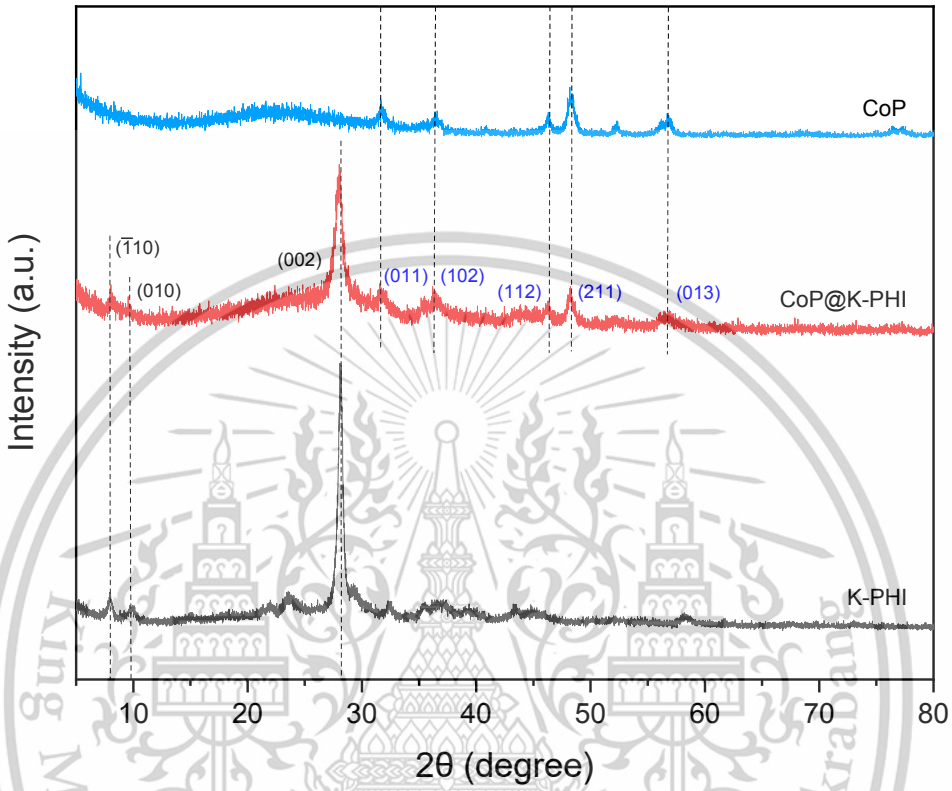

Figure 2 XRD pattern of CoP, K-PHI and CoP@K-PHI.

Figure 3 depicts the FTIR spectra of K-PHI and CoP@K-PHI to confirm the chemical structure and similarities of the prepared catalysts. In both K-PHI and CoP@K-PHI, the sharp peak at 805 cm^{-1} indicated the vibration modes of the triazine group unit [42,43] and strong absorption peaks at 1100-1700 cm^{-1} resulted from the stretching modes of heterocyclic compounds [43]. Various characteristic signals of K-PHI were presented, including the vibration mode of the C–N observed at 914 and 991

cm^{-1}. The peak at 2175 cm^{-1} can be ascribed to the stretching vibration of terminal cyano group (C≡N) [44,45], which was related to the defects in the heptazine units in K-PHI. These defects typically occurred during molten salt synthesis [46]. Additionally, the broad absorption peak positioned at 2950-3600 cm^{-1} represented the N-H stretching vibration or O-H bands involved in uncondensed amino groups and adsorbed water molecules [47,48]. However, although the similar patterns and positions of the peaks from the both catalysts were observed, the lower intensity peaks of CoP@K-PHI compared to K-PHI can be observed. This is attributed to the interaction of CoP with K-PHI via π–π interactions [49].

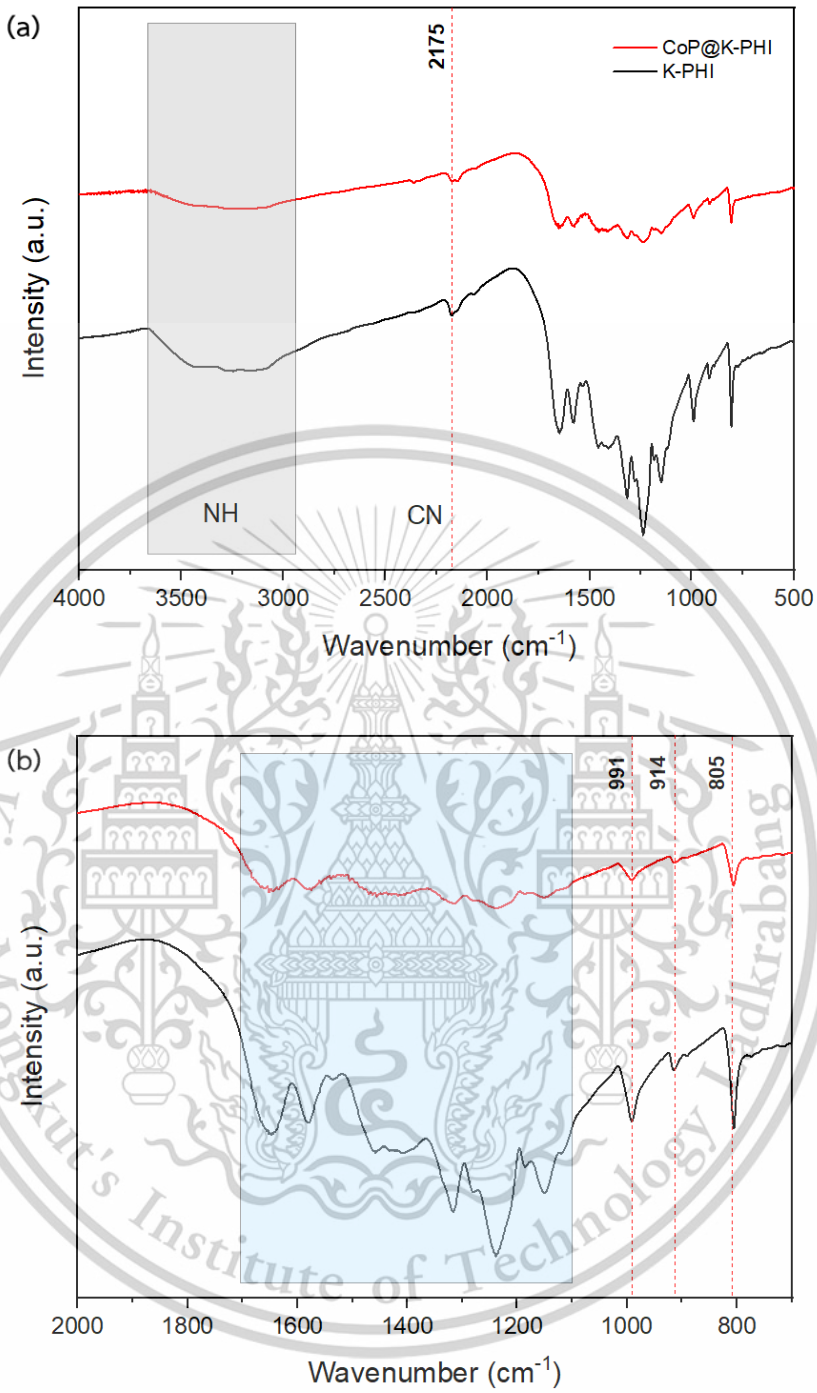

Figure 3 (a) FTIR spectra of K-PHI and CoP@K-PHI (b) Zoom view of FTIR spectra reveals the wavelength range of 700-2000 cm^{-1} of K-PHI and CoP@K-PHI.

X-ray photoelectron spectroscopy (XPS) was employed to analyze the chemical states and elemental compositions of K-PHI and CoP@K-PHI catalysts. In Figure 4a, the survey scan spectra of CoP@K-PHI indicated the presence of six elements including C, K, N, O, Co and P, whereas Co and P elements were not detected in K-PHI. From the C 1s XPS spectra (Figure 4b), both K-PHI and CoP@K-PHI displayed a major peak at a binding energy of 288.2 eV attributed to the sp^2-hybridized carbon (N–C=N) in the heptazine units and a minor peak at 288.6 eV corresponding to the cyano group (C≡N), resulting from the decomposition or incomplete polymerization during synthesis, which wass consistent to the FTIR results. In addition, the 2 peaks located at 295.6 eV and 292.8 eV were related to K $2p_{1/2}$ and K $2p_{3/2}$, respectively. These peaks from the K 2p chemical state reveal the interposition of K^+ ions in the K-PHI framework [45,46]. Figure 4c. illustrates the N 1s XPS spectra of both K-PHI and CoP@K-PHI catalysts. The prominent peak at 398.6 eV was ascribed to the sp^2-hybridized nitrogen (C−N=C) in heptazine units. Small peaks at 400.1 and 401 eV were related to tertiary nitrogen groups (N-$(C)_3$) and terminal amino groups (C−N−H). These peaks represented the basic substructure units in the formation of the K-PHI catalyst [50]. For CoP@K-PHI, 3 peaks can be observed in the Co 2p XPS spectra (Figure 4d.). The peak at 781.4 eV was Co $2p_{3/2}$ with the satellite peak located at 785.2 eV belonging to oxidized cobalt species, while the peak at 778.1 eV corresponded to the binding energy of Co–P bond in CoP [51,52]. The P 2p XPS spectra (Figure 4e) show 2 peaks at 129.2 eV and 133.6 eV, which can be attributed to P $2p_{3/2}$ of CoP and oxidized phosphate species, respectively [51]. XPS results supported the presence of CoP and successful synthesis of the K-PHI and CoP@K-PHI catalysts

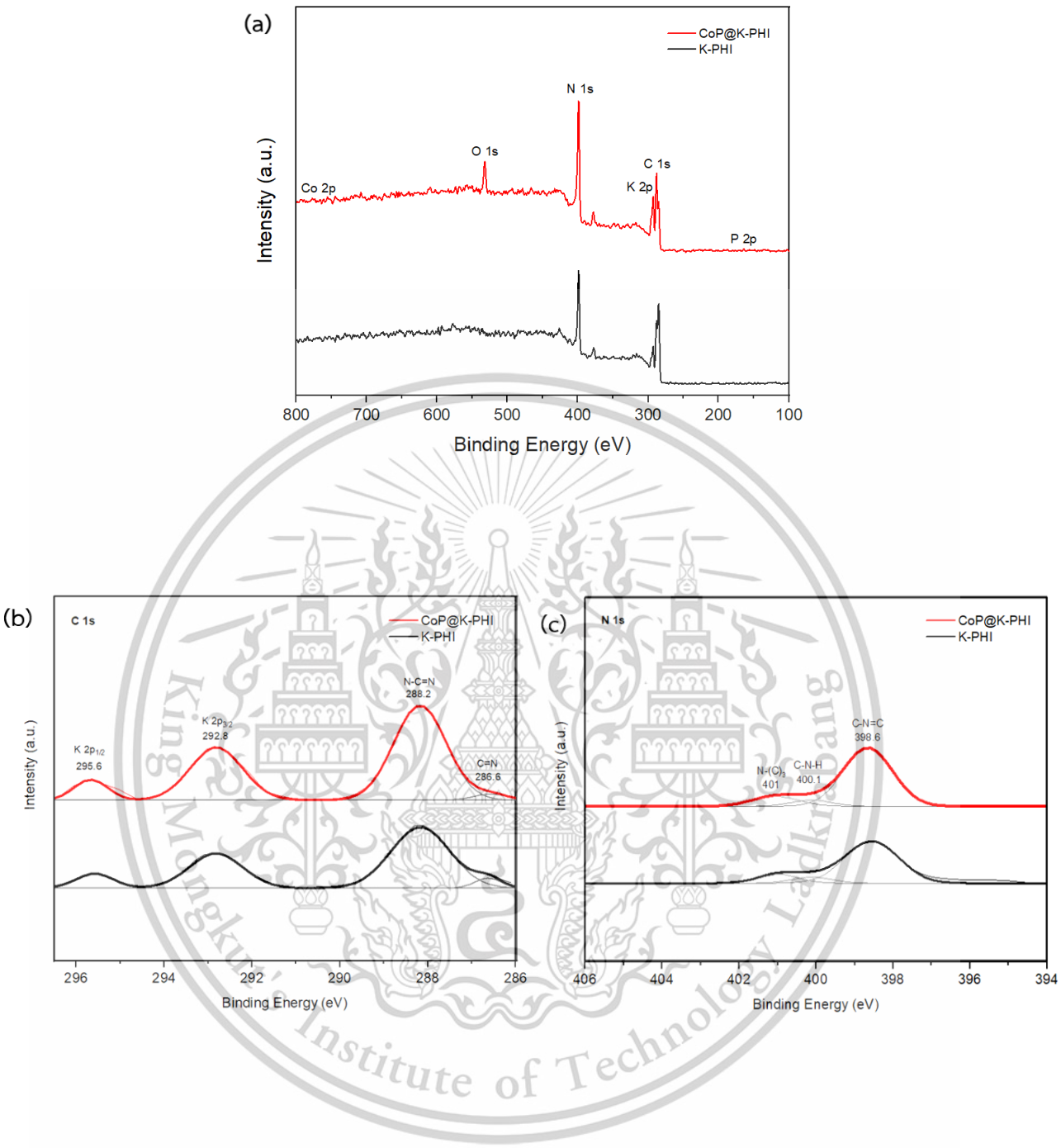

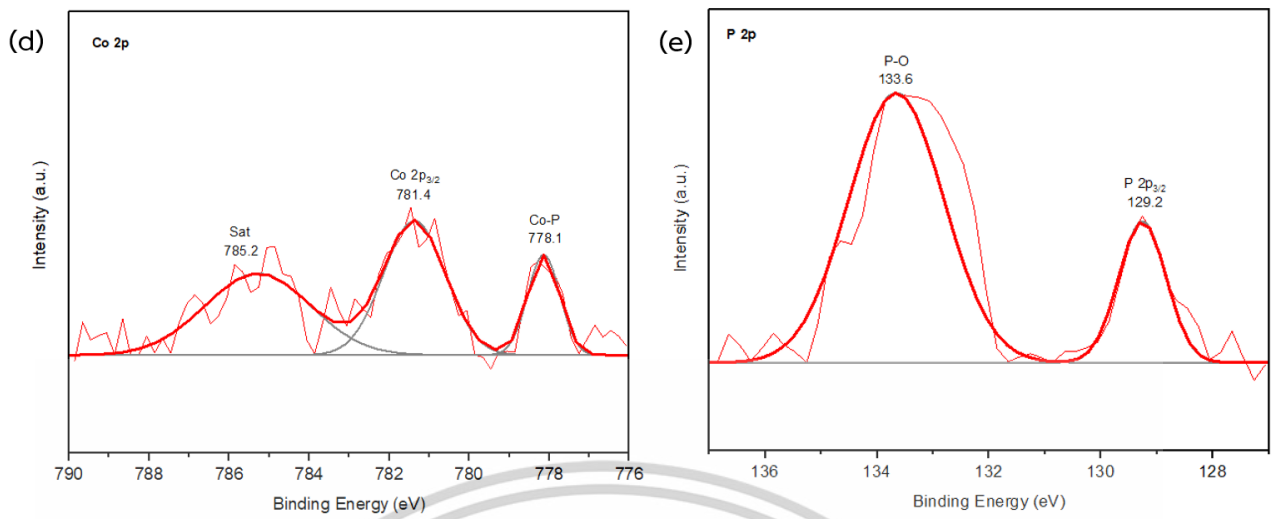

Figure 4 High resolution XPS spectra of (a) Survey (b) C 1s (c) N 1s of K-PHI and CoP@K-PHI (d) Co 2p and (e) P 2p of CoP@K-PHI.

3.2 Optical and Photophysical Properties of Photocatalysts

UV-Vis absorption and PL spectra were conducted to investigate the optical properties of the K-PHI, CoP@K-PHI and Pt@K-PHI. Figure 5 displays the UV-Vis spectra of the prepared catalyst. The band gap value was determined based on the Tauc plots in Figure 6. As a result, all catalysts exhibited an absorption edge at ~460 nm. The increased absorption intensity, which implied the efficiency for using solar irradiation in the photocatalytic reaction, in the entire visible light region of CoP@K-PHI and Pt@K-PHI compared to K-PHI demonstrated that CoP and Pt co-catalyst can improved light absorption ability of K-PHI. Furthermore, the absorption edge of CoP@K-PHI and Pt@K-PHI did not significantly shift after loading co-catalyst

indicating that CoP and Pt did not affect the internal crystal structure of K-PHI [53], which was in good agreement with the XRD results.

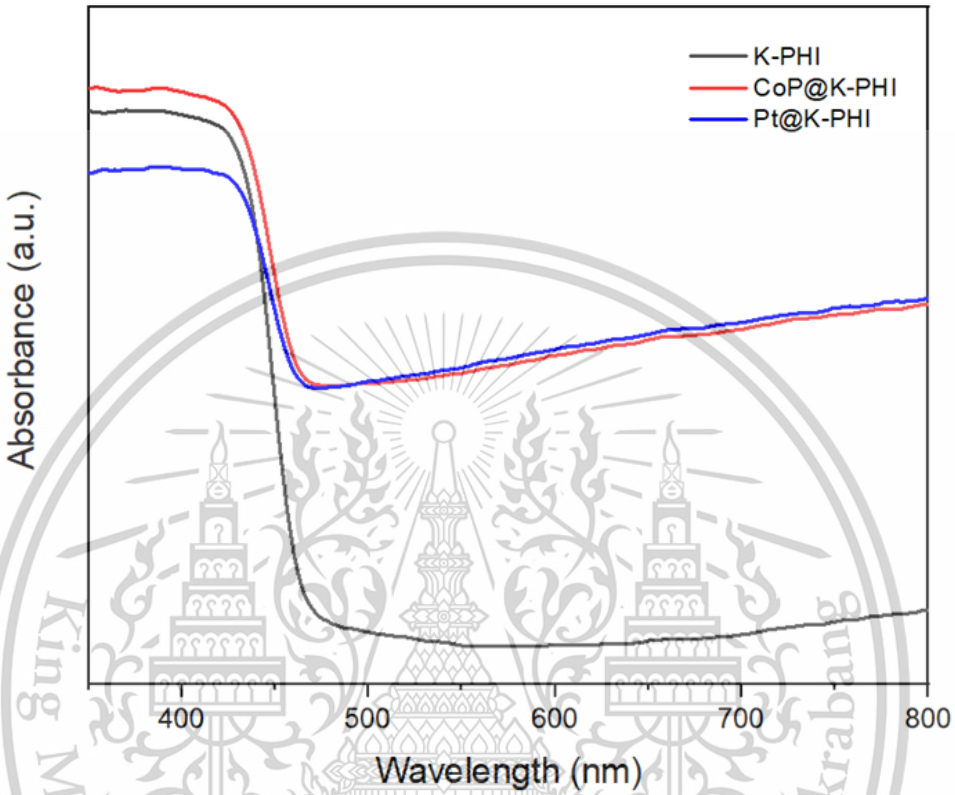

Figure 5 UV-Vis absorption spectra of K-PHI, CoP@K-PHI and Pt@K-PHI.

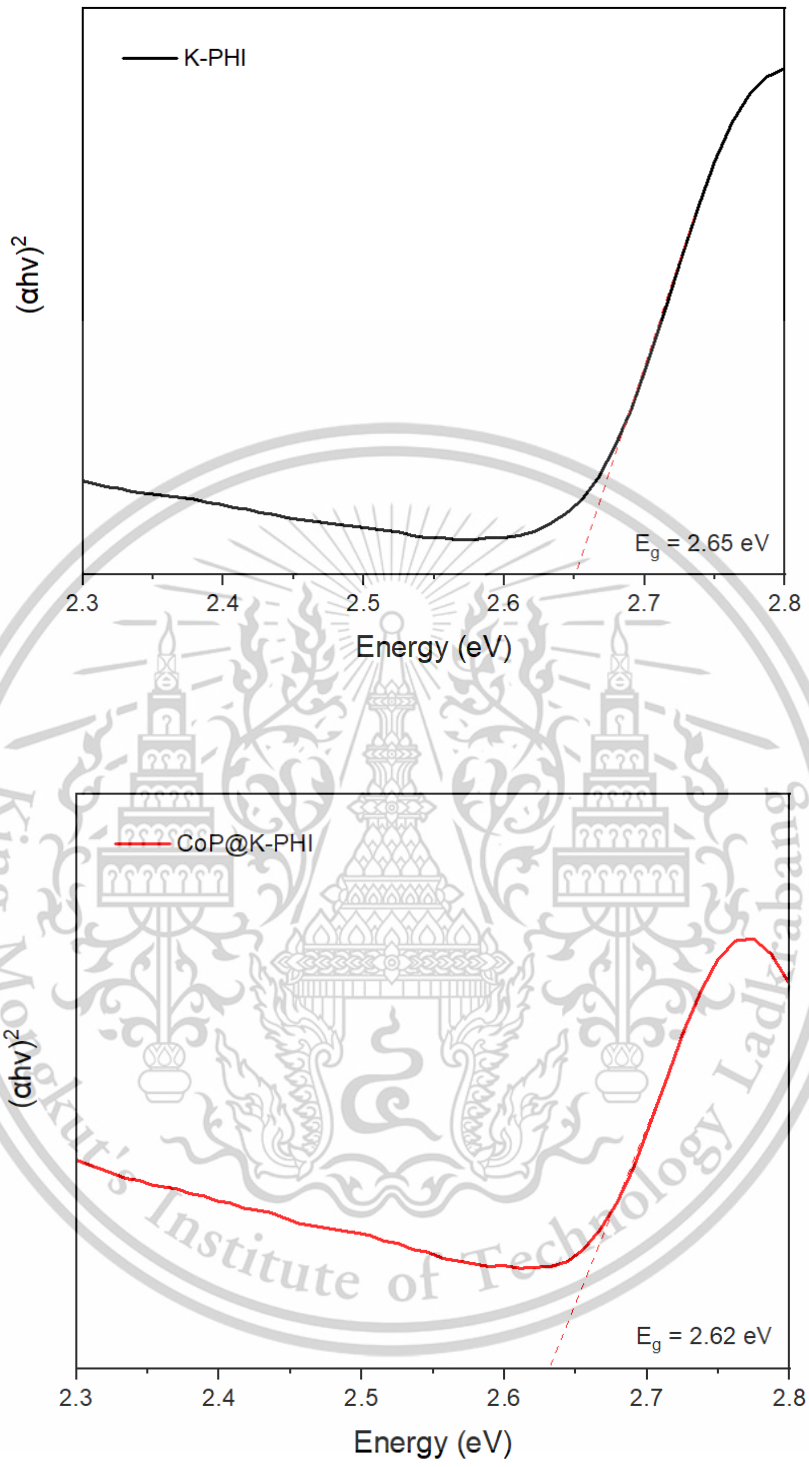

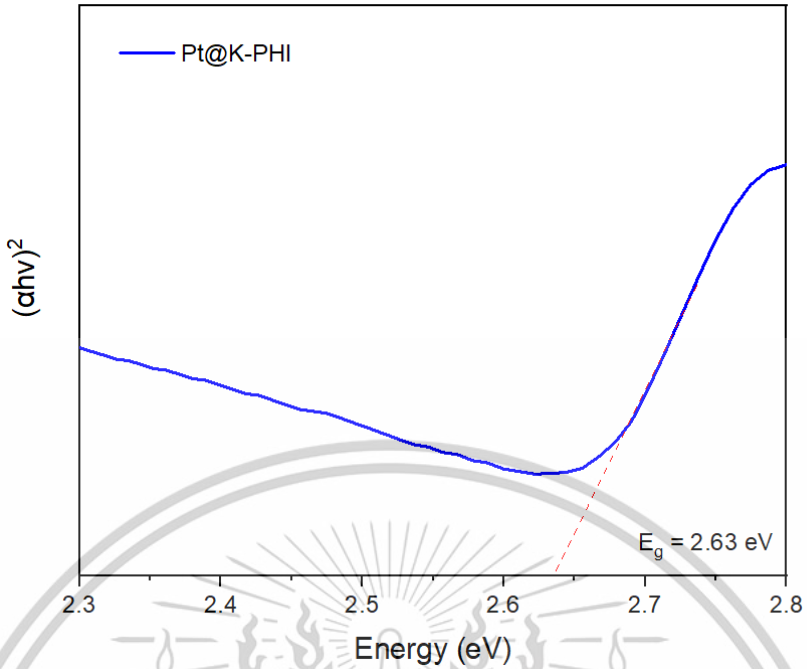

Figure 6 Tauc plots obtained from the absorption spectra of K-PHI, CoP@K-PHI and Pt@K-PHI.

The steady-state photoluminescence (PL) spectra under 325 nm excitation of K-PHI, CoP@K-PHI and Pt@K-PHI catalysts are shown in Figure 7. The PL spectrum revealed an emission peak at approximately 460 nm. The lower PL intensity of CoP@K-PHI and Pt@K-PHI compared to K-PHI indicated that loading co-catalysts into the K-PHI help increase the separation and migration efficiency of photogenerated charge carriers of the catalyst, resulting in the suppression of the internal recombination [54,55,56]. These enhancements in light absorption and charge transfer-separation contributed to improved photocatalytic activities for both hydrogen evolution and methanol reforming [57].

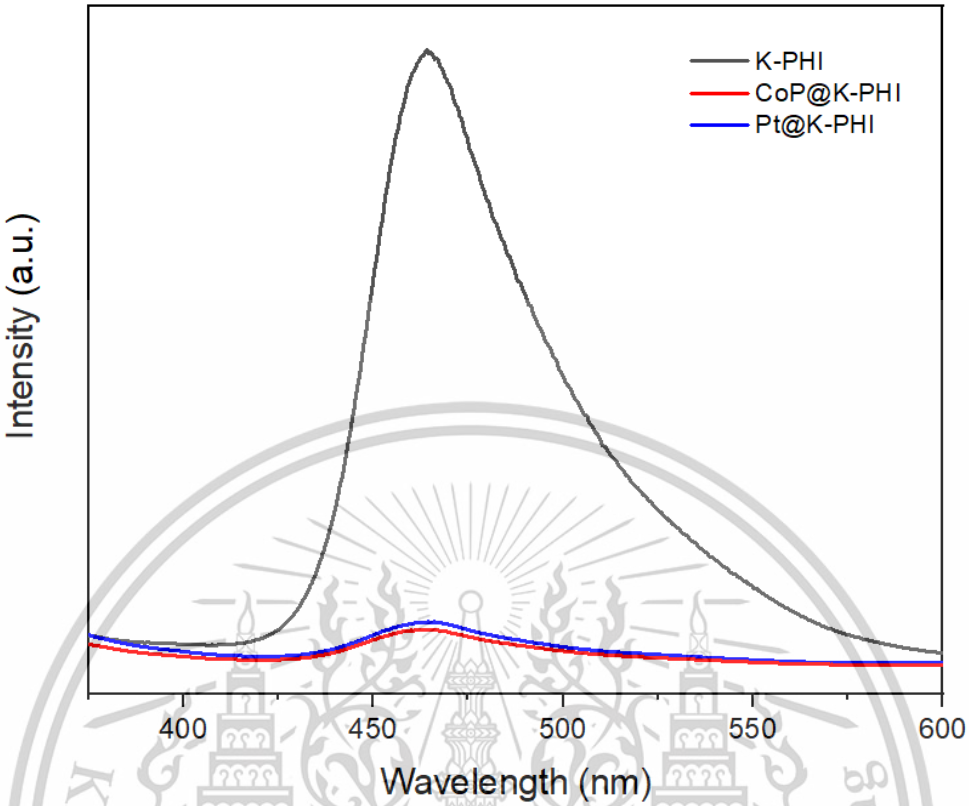

Figure 7 Steady-state PL spectra under 352 nm excitation of K-PHI, CoP/K-PHI and Pt/K-PHI.

The electronic structure of photocatalysts is crucial for determining the feasibility of photogenerated charge transfer, thereby controlling the photocatalytic redox processes and influencing the overall reaction performance. Figure 8 presents the ultraviolet photoelectron spectroscopy (UPS) spectrum of K-PHI, CoP@K-PHI and Pt@K-PHI, which was used to identify the valence band maximum (VBM) level against the vacuum. The conduction band minimum (CBM) levels of these photocatalysts were assessed based on the VBM levels and bandgap energy obtained

from the Tauc plots. As shown in the schematic energy-level diagrams of the photocatalysts relative to the levels of H_2O reductions and OH^- oxidations in an aqueous solution (Figure 9), the VBM levels of the K-PHI, CoP@K-PHI and CoP/K-PHI were -6.14 eV, -5.84 eV and -5.77 eV, respectively. The CBM levels of the photocatalysts were sufficiently high to enable the reduction of H_2O by photogenerated electrons, leading to H_2 production. Incorporating the co-catalysts increased the CBM levels and decreased the bandgap energy of K-PHI, thus enhancing the photocatalytic efficiency. These changes suggested that the co-catalysts played a significant role in modifying the electronic properties of K-PHI, resulting to be more effective for photocatalytic applications [58,59].

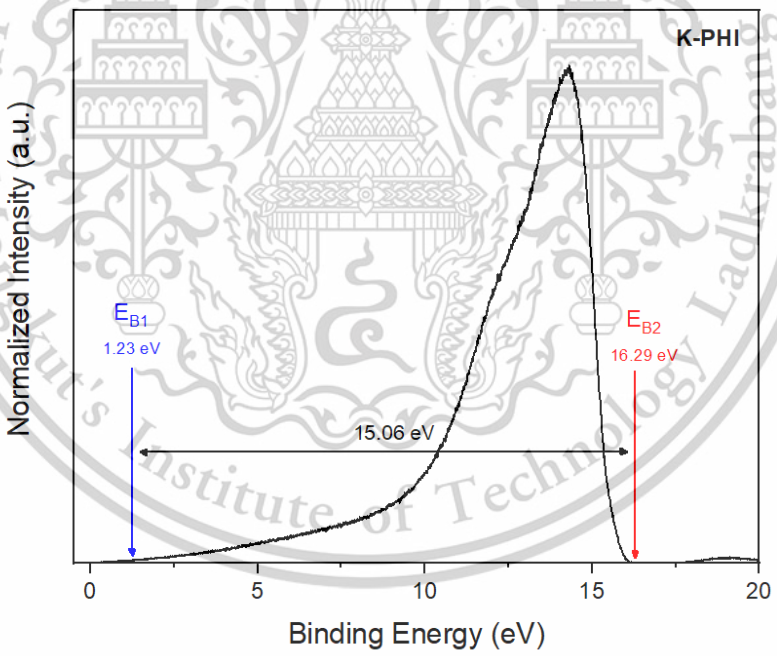

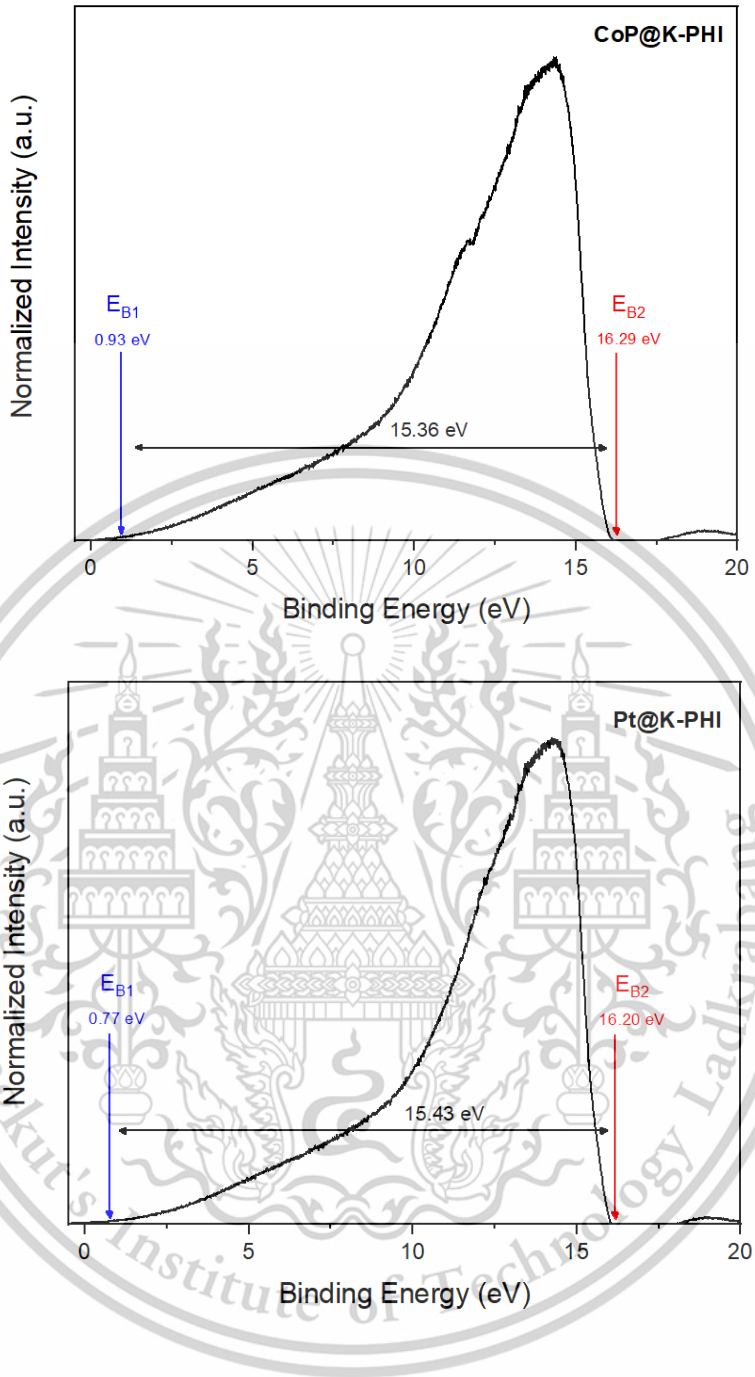

Figure 8 UPS spectra of K-PHI, CoP@K-PHI and Pt@K-PHI. The UPS widths (black lines) can be determined by these two intercept binding energies, and the VB can be calculated by subtracting these widths from the excitation energy (21.2 eV).

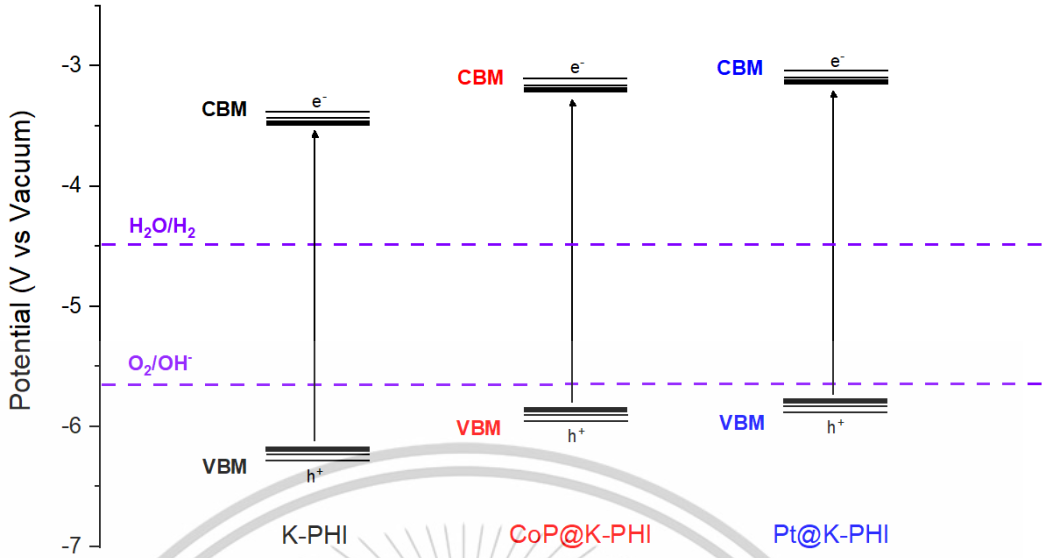

Figure 9 Schematic energy-level diagrams of the K-PHI, CoP@K-PHI and Pt@K-PHI relative to the levels of H_2O reductions and OH^- oxidations in an aqueous solution.

3.3 Photocatalytic Reforming of Methanol

Photocatalytic reforming of methanol using CoP@K-PHI compared with Pt@K-PHI was performed under the reaction conditions presented in experimental section (Chapter 2). GC-MS was used to analyze the liquid phase product from this photocatalytic reaction. Figures 10 and 11 present the GC-MS spectra of the solution after 96 h reaction period using CoP@K-PHI and Pt@K-PHI as photocatalysts, respectively. The spectrum indicated that ethylene glycol ($C_2H_4(OH)_2$) was the only product formed in the solution when CoP@K-PHI was employed in the reforming reaction. In contrast, the use of Pt@K-PHI led to the formation of acetate (CH_3COO^-),

demonstrated that the difference of co-catalyst significantly influenced the reaction pathway and the resulting product. The structures of products were confirmed through MS analysis with electron impact ionization, which identified acetic acid (m/z =60) as a product while using Pt@K-PHI and ethylene glycol (m/z =62) for CoP@K-PHI. For the gas phase, H_2 was the only product detected in the GC profile during the photoreforming process.

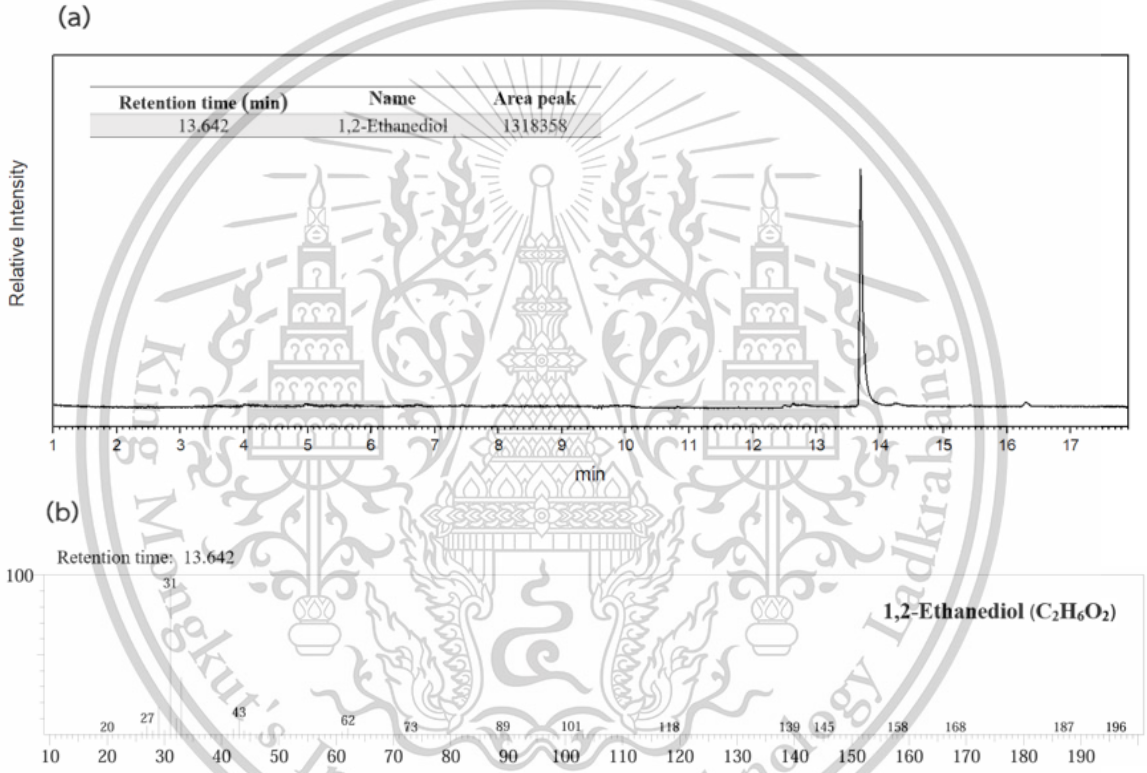

Figure 10 (a) Liquid products from the GC-MS analysis in the solution of methanol photoreforming containing CoP@K-PHI after 96 h irradiation. (b) Mass spectra of the compounds obtained from GC spectra with CoP@K-PHI. All the compounds have been confirmed with the standard solutions.

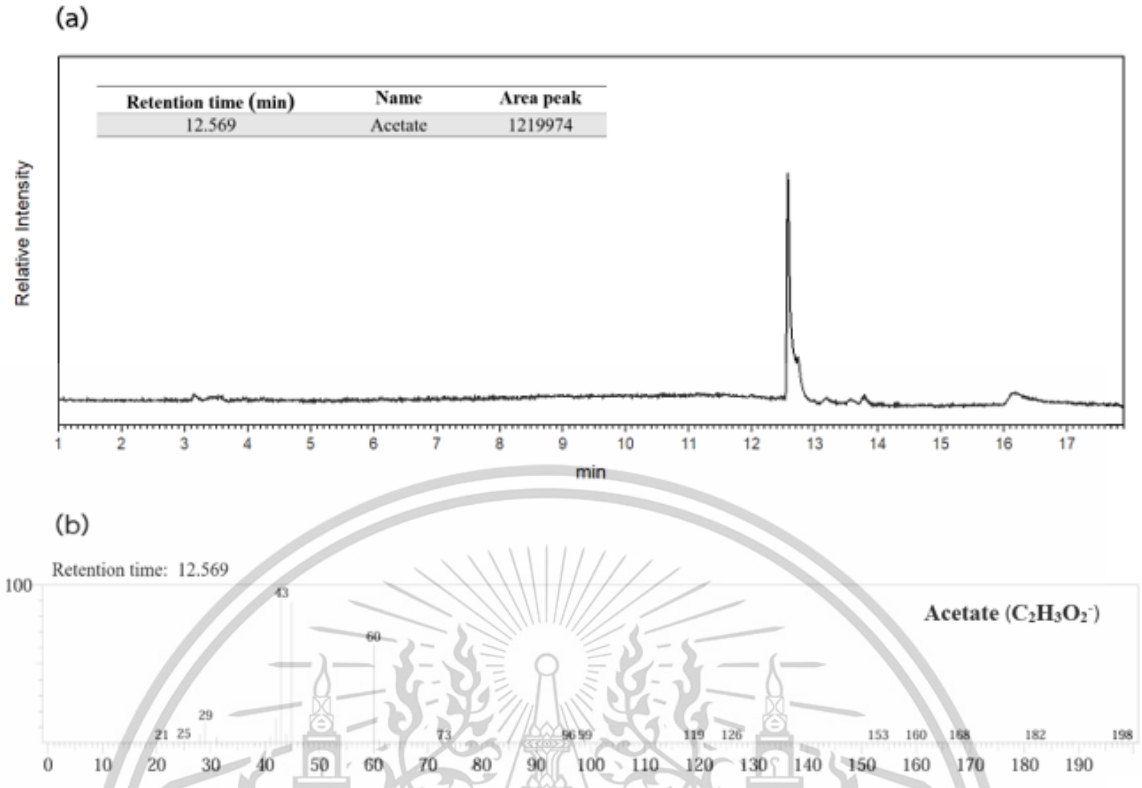

Figure 11 (a) Liquid products from the GC-MS analysis in the solution of methanol photoreforming containing Pt@K-PHI after 96 h irradiation. (b) Mass spectra of the compounds obtained from GC spectra with Pt@K-PHI. All the compounds have been confirmed with the standard solutions.

Figure 12 illustrates the reaction products, which were analyzed every 12 h during 96 h of photocatalytic methanol reforming reaction using CoP@K-PHI as a photocatalyst. Ethylene glycol, the only product in the liquid phase, was rapidly produced in substantial quantities during the first 12 h (258 μmol h^{-1}) and the production rate gradually decreased to a stable level of approximately 109 μmol h^{-1} after 24 h. Similarly, HER activity in the gas phase exhibited a similar reaction trend, with a production rate of 218 μmol h^{-1} during the first 12 h and gradually decreased to be 123 μmol h^{-1} after 24 h. In comparison, Figure 13 depicts the reaction products over the same duration using Pt@K-PHI as a photocatalyst. In addition to the difference in the liquid phase product, it was evident that the reaction trends differed significantly between 2 co-catalysts. During the first 12 h, the production rates of acetate in the liquid phase and hydrogen in the gas phase were relatively low, at 59 μmol h^{-1} and 131 μmol h^{-1}, respectively. Then, these rates gradually increased reach to the highest production rates of 101 μmol h^{-1} from acetate and 197 μmol h^{-1} from hydrogen after 60 h. The total amount of hydrogen from Pt@K-PHI was slightly higher than that from CoP@K-PHI, due to Pt was more effective in trapping photogenerated electrons for HER. However, CoP@K-PHI also demonstrated the effective performances in methanol reforming and hydrogen production. Considering the cost and product differences, CoP may emerge as a promising co-catalyst in the photocatalytic reactions. The distinct reaction trends observed may be attributed to the co-catalyst loading method into K-PHI. In the first 12 h, Pt was in the initial photodeposition progress, while CoP was pre-deposited prior to the reaction's commencement [58].

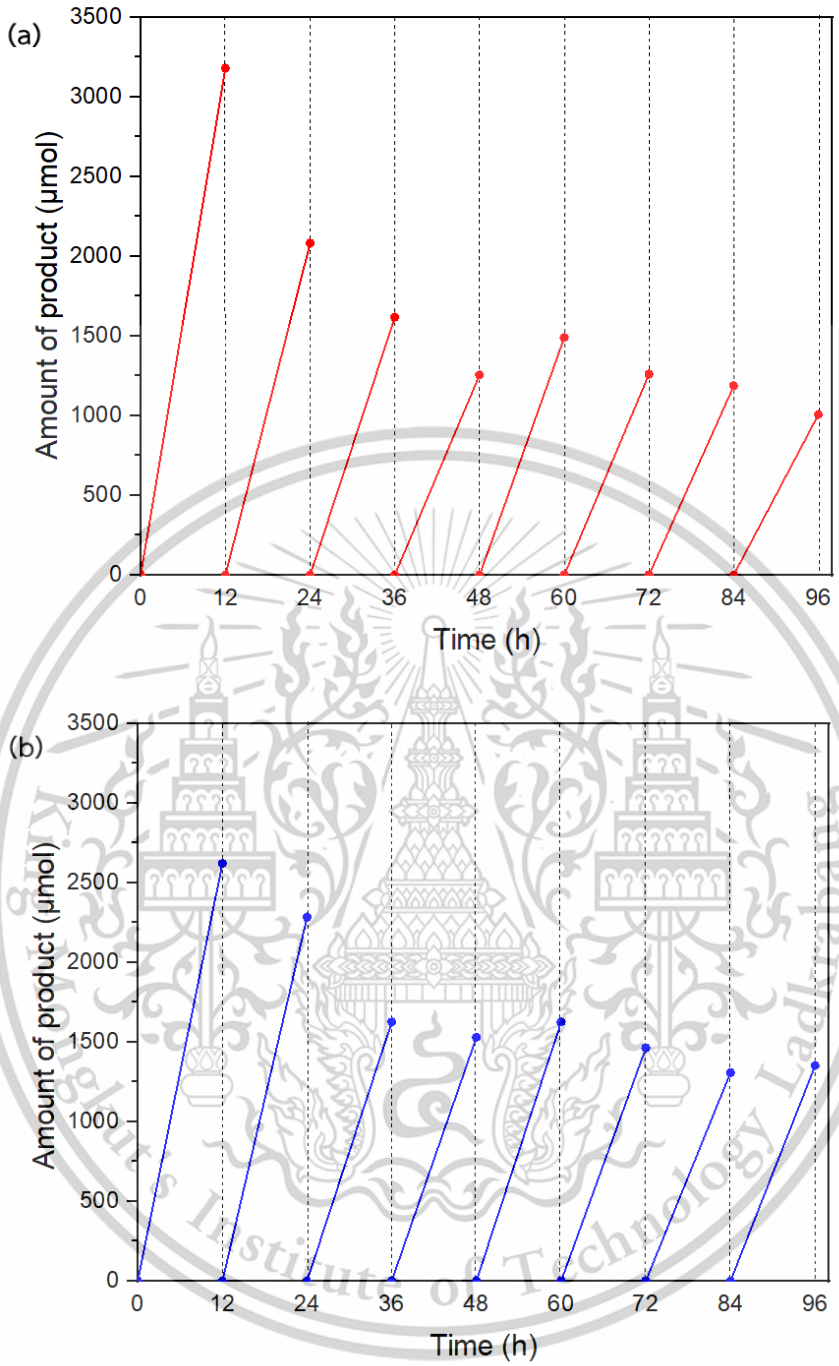

Figure 12 Productions of (a) ethylene glycol (liquid phase) (b) hydrogen (gas phase) over 12 h intervals during 96 h of photocatalytic methanol reforming with CoP@K-PHI under simulated solar irradiation.

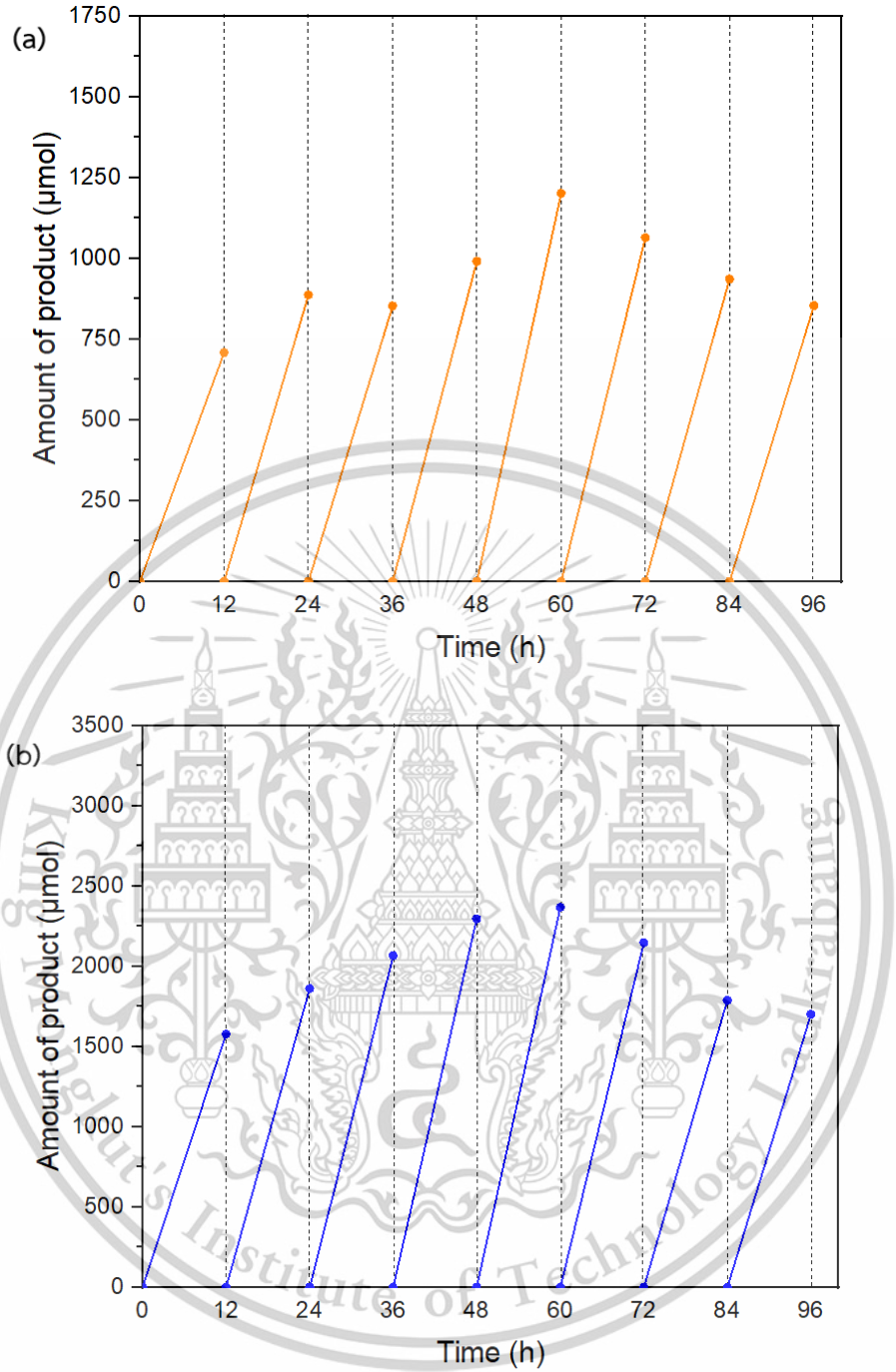

Figure 13 Productions of (a) acetate (liquid phase) (b) hydrogen (gas phase) over 12 h intervals during 96 h of photocatalytic methanol reforming with Pt@K-PHI under simulated solar irradiation.

3.4 Mechanism of Methanol Reforming over CoP@K-PHI and Pt@K-PHI

Due to the effect of different co-catalysts on the product selections in the photocatalytic reforming of methanol, the associated free radicals and the functional roles of CoP and Pt co-catalysts were studied by analyzing the reaction pathways via electron paramagnetic resonance (EPR). Figures 14 and 15 display EPR signals using 5,5-dimethyl-1-pyrroline-N-oxide (DMPO) as the spin trapping agent to further explore the formation of the intermediate free radicals in the photocatalytic methanol reforming reaction using CoP@K-PHI and Pt@K-PHI as photocatalysts, respectively. The spectrum of the solution with CoP@K-PHI after 1 min of irradiation (Figure 14a) revealed signal patterns of the adducts DMPO–•CH_2OH, DMPO–•H and DMPO–•OH, consistent with documented reference spectra (Figure 14b). In contrast, the spectrum of Pt@K-PHI (Figure 15a) showed significantly different intermediate free radical formations, exhibiting the signal patterns of the adducts DMPO–•CH_3, DMPO–•CO_2^-, DMPO–•H and DMPO–•OH, also consistent with the documented reference spectra (Figure 15b) [59,60,61]. The generation of free radicals indicated that •H and •OH radicals might have been produced from H_2O reduction and oxidation of OH^- in the photocatalytic reaction, respectively. The •CH_3 and •CO_2^- radicals observed in the solution using Pt@K-PHI co-catalyst were generated from the photocatalytic dehydration of methanol with reactive •H and •OH, respectively [59]. The •CH_2OH radical was produced from C-H bonds activation of methanol by reactive •OH. These •CH_2OH radicals were the major intermediate for the ethylene glycol production [62,63]. Thus, it was evident that the photoholes and •OH from the oxidation reaction

played a crucial role in ethylene glycol production from the photocatalytic reforming of methanol using CoP@K-PHI.

The modification of co-catalysts into K-PHI could significantly enhance the efficiencies of photocatalytic H_2 production and methanol reforming reactions with the different roles, resulting in different reaction pathways and selective product formations. The CoP co-catalyst may provide the active sites to promote hole trapping and the selective cleavage of inert C-H bonds of methanol subsequent C-C coupling of $\bullet CH_2OH$ radicals to produce the ethylene glycol. Additionally, the photogenerated charge separation and migration efficiency of CoP influence the coupling of •H radicals to produce H_2 on the K-PHI surface. Conversely, Pt acts as an effective co-catalyst to act as H_2O reduction sites with electrons to facilitate H_2 production and subsequently improve the photocatalytic C-C coupling reaction to produce acetate [62,64].

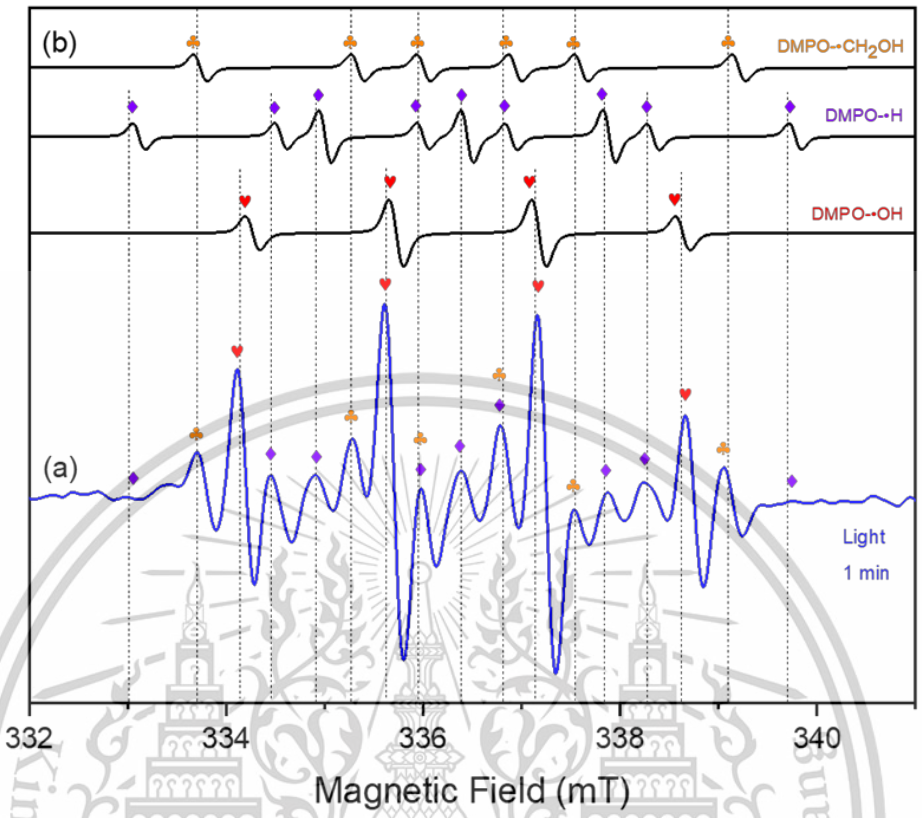

Figure 14 Analysis of free radicals by employing spin trapping by DMPO and subsequent analysis through EPR. (a) EPR spectrum captures the spin-trapping adducts from the photocatalytic methanol reforming with CoP@K-PHI after 1 min irradiation. (b) Documented EPR spectra of spin-trapped species, DMPO–•CH_2OH, DMPO–•H and DMPO–•OH.

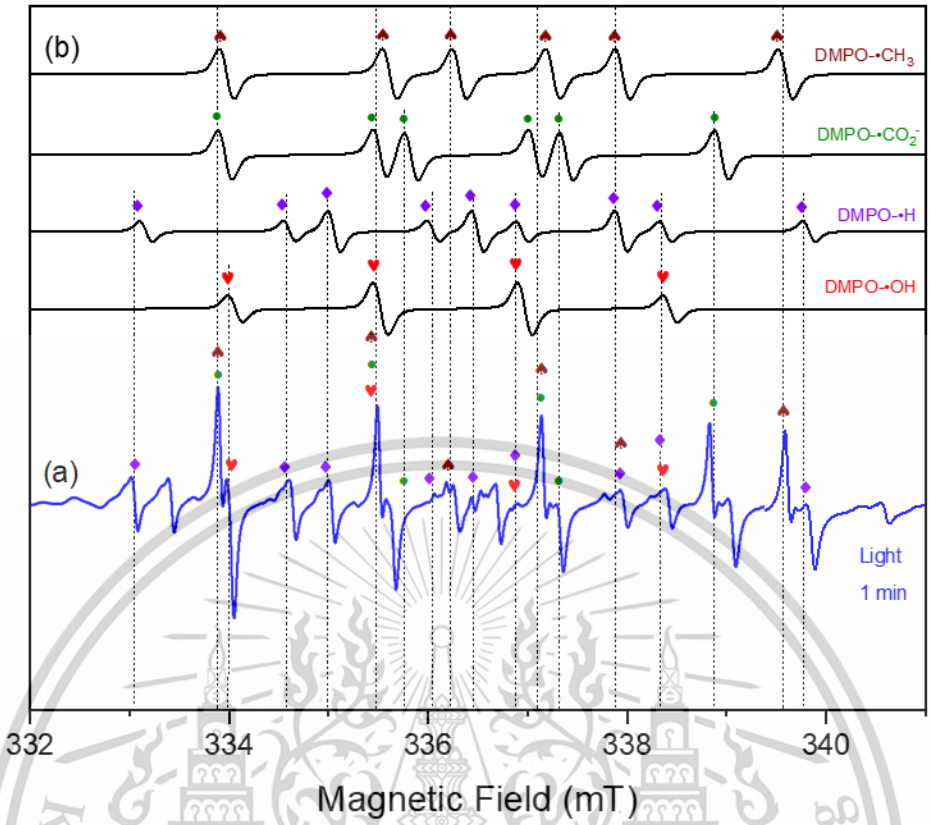

Figure 15 Analysis of free radicals by employing spin trapping by DMPO and subsequent analysis through EPR. (a) EPR spectrum captures the spin-trapping adducts from the photocatalytic methanol reforming with Pt@K-PHI after 1 min irradiation. (b) Documented EPR spectra of spin-trapped species, DMPO–•CH_3, DMPO–•CO_2^-, DMPO–•H and DMPO–•OH.

Figure 16 illustrates the reaction pathways involved in the photocatalytic hydrogen evolution reaction (HER) and the reforming of methanol into ethylene glycol using CoP@K-PHI as a photocatalyst. Under irradiation, the process initiated with the absorption of light by K-PHI exciting electrons in the valence band (VB) to the conduction band (CB), so the holes were left in the valence band. These photogenerated electrons participated in the reduction of H_2O, leading to the formations of OH^- and •H. The •H radicals on the K-PHI surface participate in coupling to produce H_2 [65,66]. Along with the photocatalytic reduction, photogenerated holes from K-PHI migrated to the CoP co-catalyst and combined with OH^- to form reactive •OH species, which efficiently activated the C-H bonds of methanol. The $•CH_2OH$ radicals produced from the C-H bond activation of methanol underwent C-C coupling to form ethylene glycol which was the valuable product of this photocatalytic methanol reforming reaction [62]. CoP served as an effective co-catalyst by providing active sites for the transfer and assembly of photogenerated holes from K-PHI preventing the charge carrier recombination and allowing a higher concentration of electrons accumulated on the K-PHI surface for enhancing H_2O reduction reactions, thereby improving the HER process [67].

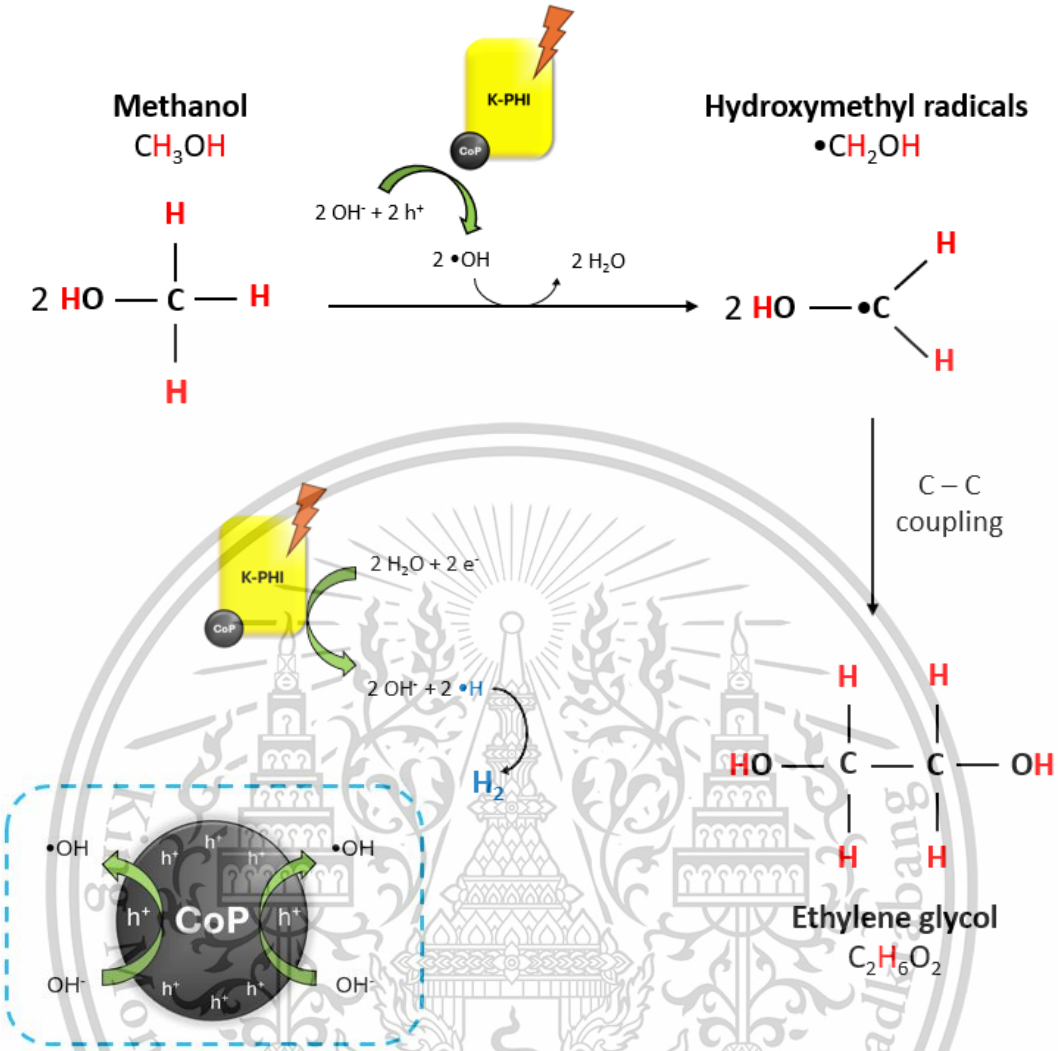

Figure 16 Proposed mechanism in the photocatalytic reforming of methanol over CoP@K-PHI to produce ethylene glycol and functional role of the CoP co-catalyst.

Figure 17 shows the distinct reaction pathways and the functional role of the Pt co-catalyst in the photocatalytic reforming of methanol. Pt has been well-recognized for its efficiency in photocatalytic H_2O reduction by trapping photogenerated electrons from K-PHI to generate •H radicals, which subsequently couple to produce H_2 [15,67]. In addition to hydrogen production, the reactive •H radicals formed on the Pt co-catalyst through the interaction of photogenerated electrons and H_2O were also responsible for photocatalytic dehydration of methanol. These •H radicals attacked the C-OH bond in methanol, leading to the formation of $•CH_3$ radicals. Concurrently, the effective charge carrier separation and transfer facilitated by the Pt co-catalyst resulted in a large number of holes accumulation on the K-PHI surface, which was sufficient to produce the reactive •OH radicals through the photooxidation of OH^-. These •OH radicals contributed to the reforming of methanol via photocatalytic dehydration, resulting in the formation of $•CO_2^-$ radicals [59]. The generated $•CH_3$ and $•CO_2^-$ radicals subsequently underwent C-C coupling to produce acetate as the valuable product of this photocatalytic reaction. However, the presence of intermediates such as formaldehyde or formate could not be detected in our analysis, suggesting that the reaction proceeded rapidly.

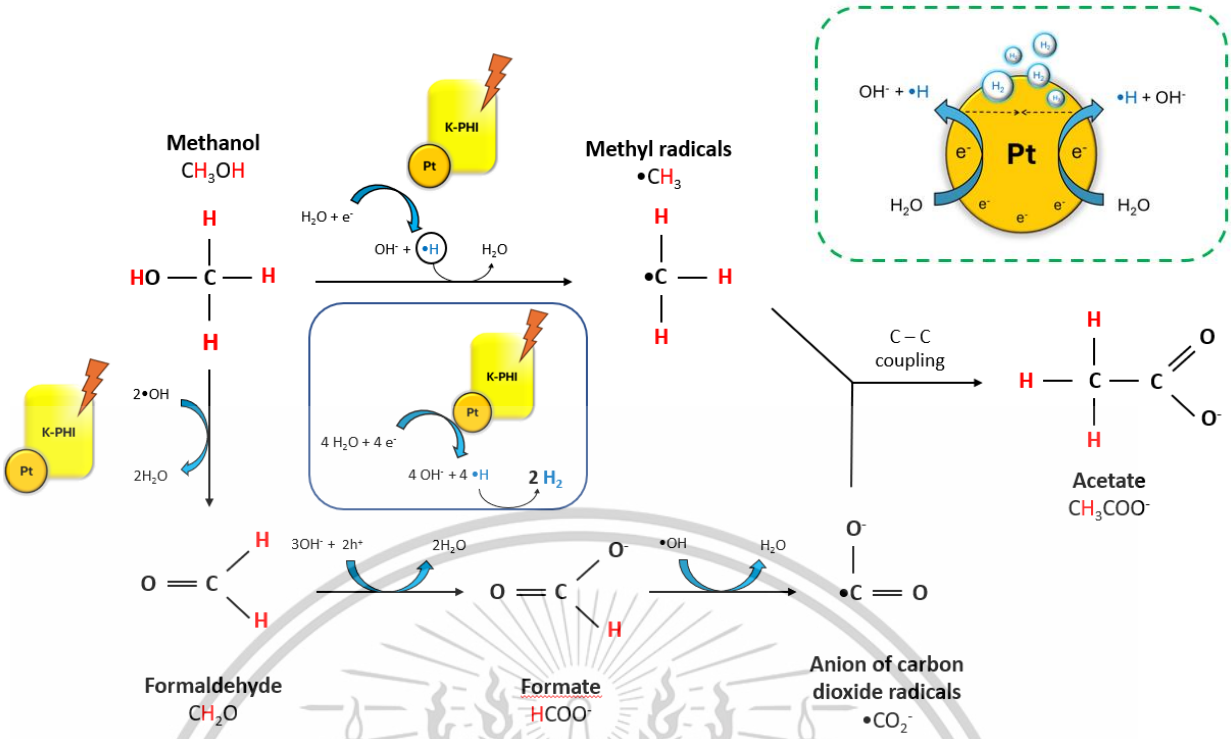

Figure 17 Proposed mechanism in the photocatalytic reforming of methanol over Pt@K-PHI to produce acetate and functional role of the Pt co-catalyst.

Table 1 provides a comparative analysis of recent studies on photocatalytic methanol reforming reactions, focusing on key parameters such as the photocatalyst used and experiment conditions resulted to the reforming products, conversion rates, and selectivity. These parameters are crucial for evaluating the efficiency and practicality of photocatalytic processes, as they reveal the influence on specific reaction pathways, product selection, and overall performance. By summarizing these findings, the table highlights current advancements, identifies variations in outcomes, and pinpoints knowledge gaps in the field, offering a foundation for optimizing photocatalytic systems.

Table 0 Literature review on photocatalytic methanol reforming reaction.

Photocatalyst	Experiment conditions	Irradiation source	Reforming product	Conversion	Main product selectivity	Ref.
CoP@K-PHI	225 mL of H_2O + 25 mL of CH_3OH	Solar simulator	Ethylene glycol	2.3%	100%	This work
Pt@K-PHI	225 mL of H_2O + 25 mL of CH_3OH	Solar simulator	Acetate	1.2%	100%	This work
Pt/TiO_2	1 L of CH_3OH	UV irradiation	Formaldyhyde, Methyl formate	-	56.1–100% depend on operation temperature	[20]
$CoP/Zn_2In_2S_5$	5.0 cm^3,76 wt% CH_3OH + 24 wt% H_2O	300 W Xenon lamp; visible light (λ = 400-780 nm)	Ethylene glycol, Formaldehyde	4.5%	90%	[64]
Pt/TiO_2	Photo-steam reforming reactor recirculation mode with 40 mL min^{-1} of a 2% CH_3OH/3% H_2O/N_2 (balance) gas mixture	Iron halogenide mercury arc lamp (λ = 350-400 nm)	Formaldehyde, Formic acid	-	38.5%	[71]
Ag/TiO_2			Formaldehyde, Formic acid	-	98.8%	[71]
Au/TiO_2			Formaldehyde, Formic acid	-	38.9%	[71]
$Au-Ag/TiO_2$			Formaldehyde, Formic acid	-	40.9%	[71]
Pd/TiO_2	0.5 mL D_2O + 20 µL CH_3OH	Xenon lamp (350 nm $\leq \lambda \leq$ 400 nm)	Methyl glycol, Hemiacetal, Formic acid	-	-	[72]
Cu/TiO_2	50 mL CH_3OH solution	300 W Xenon lamp	Formaldyhyde	-	100%	[73]
Ni/CdS	CH_3OH solution	300 W Xenon lamp (λ > 420 nm)	Formaldyhyde	-	100%	[74]

Photocatalyst	Experiment conditions	Irradiation source	Reforming product	Conversion	Main product selectivity	Ref.
g-C_3N_4/$LaCoO_3$	100 mL 5 vol% CH_3OH solution	300 W Xenon lamp (λ = 450 nm)	Methane	-	100%	[75]
Bi_2WO_6, BiOBr, Bi_2MoO_6, $BiVO_4$	100 mL CH_3OH solution	300 W halogen tungsten projector lamp	Formaldyhyde	-	-	[76]
Pt/TiO_2	CH_3OH solution	300 W Xenon lamp (λ = 420 nm)	Formaldyhyde, Methylene glycol, Methoxymethanol	-	-	[77]
TiO_2	CH_3OH solution	300 W Xenon lamp	Methoxymethanol, Methylene glycol, Methyl formate	-	-	[78]
Pt-Nb/TiO_2	30 vol% CH_3OH solution	Hg-Xe lamp and dichroic filters allowing exposure of the catalysis to the UV (280–400 nm)	Formic acid, Formaldehyde, Methyl formate	-	85%	[79]
Pt-Nb/TiO_2	30 vol% CH_3OH solution	Hg-Xe lamp and dichroic filters allowing exposure of the catalysis to the Visible (420–680 nm)	Formic acid, Methyl formate	-	91%	[79]
CuO/TiO_2-T	1 vol% CH_3OH solution	500W Mercury lamp (λ = 365 nm), UV-Light	Methyl formate	93.3%	89.4%	[80]

Photocatalyst	Experiment conditions	Irradiation source	Reforming product	Conversion	Main product selectivity	Ref.
CuO/CuZnAl	1 vol.% CH_3OH solution	500W Mercury lamp (λ = 365 nm)	Methyl formate	80%	60%	[81]
MoS_2/CdS nanorods	76 vol.% CH_3OH solution	Xenon lamp (λ = 420-680 nm)	Ethylene glycol	-	-	[82]
2D SnS/g-C_3N_4	Pure CH_3OH	300 W Microsolar lamp	Methylal, Methylformate	-	54.3%	[83]
MgO porous nanocrystal	Pure CH_3OH	Mercury lamp (λ = 200-2500 nm)	Formaldehyde	-	-	[84]
Au NDs/ TiO_2	10 vol.% CH_3OH solution	500 W Hg-Xe arc lamp and cut-off filter (λ > 400 nm)	Formaldehyde, Formic acid,	-	-	[85]

3.5 Study of Photodegradation of Atrazine

The previous experimental results demonstrated the advantages of photocatalysts and photocatalytic processes for enhancing chemical value and producing environmentally friendly fuels. Building on this foundation, we extend our research to address environmental remediation challenges by studying the photodegradation of atrazine, a persistent and toxic herbicide widely used in agriculture [68] by focusing on the effects of solution height and the TiO_2 photocatalyst for potential practical applications. This shift explores the various benefits of photocatalytic processes—not only as a tool for clean fuel and valuable chemicals production but also as a promising approach for pollutant degradation.

The experiments were conducted in a 11.4 x 18.9 x 13.4 cm reactor containing 40 ppm atrazine dissolved in a 30:70 ratio of DI water to methanol solution using UVC lamp as the irradiation source. The concentration of atrazine in the solution was analyzed by using high performance liquid chromatography (P2000 HPLC, 223 nm UV detector, C18 QuasarTM column). Figure 18 shows the atrazine concentration during the photodegradation process without catalyst at different solution heights. After 150 min, the degradation efficiencies were approximately 47.77%, 42.66%, 39.73%, 30.77%, and 18.63% at the solution heights of 2, 3, 4, 8, and 12 cm, respectively. These results indicated that solution height significantly affects atrazine degradation efficiency. As the solution height increased, the concentration of light absorbed by atrazine molecules to enter the excited state reaction was reduced. Therefore, the

solution heights of 8 cm and 12 cm were unsuitable for this process due to the low degradation efficiency observed.

To investigate the effects of catalyst concentration, TiO_2 photocatalyst was introduced into the atrazine solution with conditions described above and stirred until homogeneous before irradiation. The TiO_2 concentrations used were 1, 2, and 4 g/L at each solution height. 1 mL samples of the solution were collected and then analyzed using HPLC. Figure 19 illustrates the atrazine concentration at different solution heights with varying amounts of TiO_2 as the photocatalyst. The presence of the TiO_2 enhanced the atrazine degradation efficiency compared to that without a catalyst reaction. At solution heights of 4 cm (Figure 19a.) and 3 cm (Figure 19b.), the degradation rates followed similar trends. The increased catalyst amounts led to improved degradation efficiency due to the effective ability of the catalyst to trap and transfer photogenerated charges. On the other hand, Figure 19c shows a distinct trend at a solution height of 2 cm by increased the amount of catalyst resulted in a decreased degradation efficiency, which was attributed to the excess catalyst. The accumulation of catalyst from the lower solution height led to faster sedimentation resulted in lower surface area and blocked the active sites of TiO_2 [69]. Additionally, the excess catalyst can scatter light at the solution surface, decreasing light penetration and subsequently reducing the energy absorbed by the atrazine molecules [70].

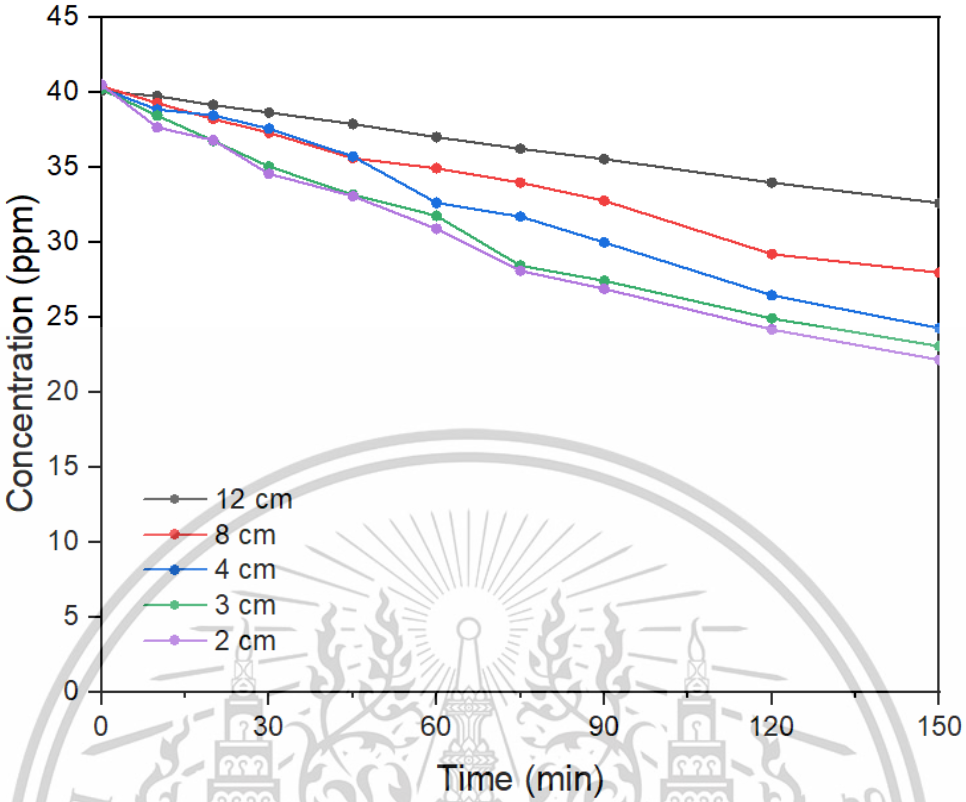

Figure 18 The concentration of atrazine in the solution during photodegradation without catalyst at the different solution heights.

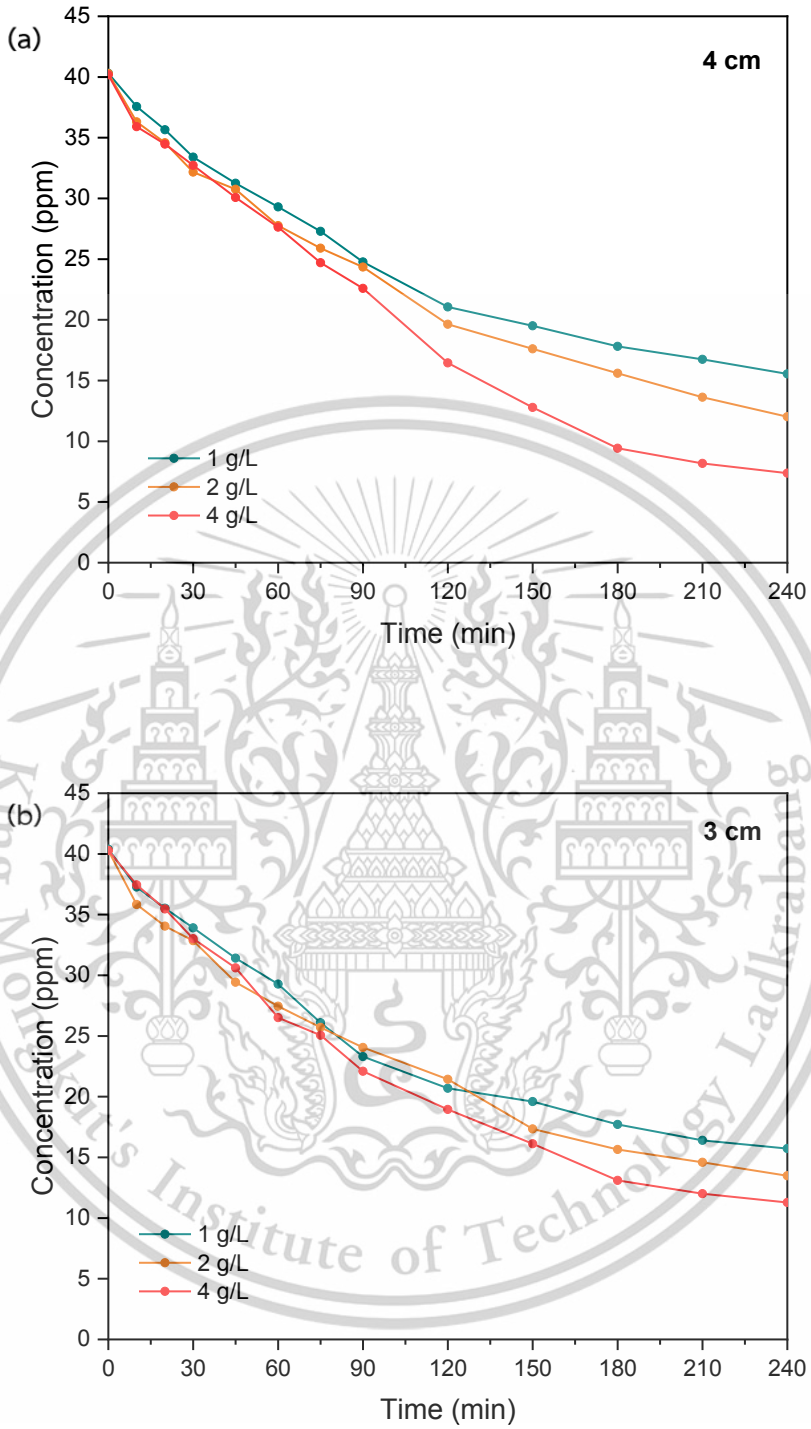

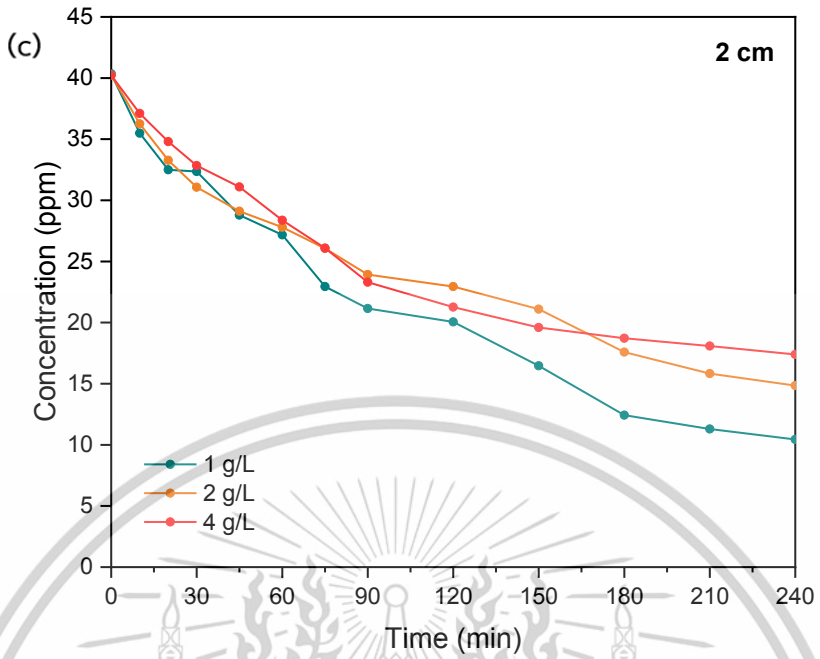

Figure 19 Photodegradation of atrazine with the different amount of TiO_2 catalyst at the height of solution (a) 4 cm (b) 3 cm (c) 2 cm.

CHAPTER 4 CONCLUSION

This study explored the photocatalytic H_2 production combined with the reforming of methanol into high-value products using K-PHI photocatalyst under solar irradiation. Our results provided significant insights into the functional roles of CoP and Pt co-catalysts in this process, particularly in influence on product selection and reaction pathways. From electron paramagnetic resonance (EPR) analysis, it was identified that the formation of various intermediate free radicals play crucial roles in determining the final products of the reaction. H_2 was the sole product in the gas phase that was generated through coupling of •H radicals. In the liquid phase, CoP@K-PHI was found to be particularly effective in promoting the selective production of ethylene glycol by generating and coupling of $•CH_2OH$ radicals. The CoP co-catalyst served as an efficient site for photogenerated charge separation and holes trapping, promoting the C-H bond activation of methanol and the subsequent C-C coupling required for ethylene glycol formation. In contrast, Pt acted as an effective co-catalyst for trapping photogenerated electrons to produce •H radicals. Pt@K-PHI facilitated the production of acetate by generating methyl ($•CH_3$) and carbon dioxide anion ($•CO_2^-$) radicals through the photocatalytic dehydration of methanol, showcasing its efficiency in hydrogen evolution reaction (HER) and methanol reforming via distinct reaction pathways.

In summary, this study revealed the potential of modifying co-catalysts to fine-tune reaction pathways and produce desired products. CoP exhibited selective ethylene

glycol production, offering a promising route for cost-effective and environmentally sustainable processes. On the other hand, Pt showed robust activity in HER, contributing to efficient hydrogen production while also facilitating acetate formation. The strategic use of co-catalysts like CoP and Pt in photocatalytic reactions could lead to significant advancements in solar fuel productions and green chemistry, with broader implications for energy and environmental sustainability.

REFEREN55CES

1. Olabi, A., & Abdelkareem, M. A. (2022). Renewable energy and climate change. Renewable and Sustainable Energy Reviews, 158, 112111.
2. Owusu, P., & Asumadu-Sarkodie, S. (2016). A review of renewable energy sources, sustainability issues and climate change mitigation. Cogent Eng 3 (1): 1167990. In.
3. Gernaat, D. E., de Boer, H. S., Daioglou, V., Yalew, S. G., Müller, C., & van Vuuren, D. P. (2021). Climate change impacts on renewable energy supply. Nature Climate Change, 11(2), 119-125.
4. Corredor, J., Rivero, M. J., Rangel, C. M., Gloaguen, F., & Ortiz, I. (2019). Comprehensive review and future perspectives on the photocatalytic hydrogen production. Journal of Chemical Technology & Biotechnology, 94(10), 3049-3063.
5. Liu, G., Sheng, Y., Ager, J. W., Kraft, M., & Xu, R. (2019). Research advances towards large-scale solar hydrogen production from water. EnergyChem, 1(2), 100014.
6. Nomikos, G. N., Panagiotopoulou, P., Kondarides, D. I., & Verykios, X. E. (2014). Kinetic and mechanistic study of the photocatalytic reforming of methanol over Pt/TiO2 catalyst. Applied Catalysis B: Environmental, 146, 249-257.
7. Wang, R., Wang, L., Zhou, Y., & Zou, Z. (2019). Al-ZnO/CdS photoanode modified with a triple functions conformal TiO2 film for enhanced photoelectrochemical efficiency and stability. Applied Catalysis B: Environmental, 255, 117738.
8. Lin, C., Song, Y., Cao, L., & Chen, S. (2013). TiO2 nanotubes/ZnO/CdS ternary nanocomposites: preparation, characterization and photocatalysis. Journal of the Chinese Advanced Materials Society, 1(3), 188-199.

9. Ong, W.-J., Tan, L.-L., Ng, Y. H., Yong, S.-T., & Chai, S.-P. (2016). Graphitic carbon nitride (g-C3N4)-based photocatalysts for artificial photosynthesis and environmental remediation: are we a step closer to achieving sustainability? Chemical reviews, 116(12), 7159-7329.
10. Nimbalkar, D. B., Nguyen, V.-C., Shih, C.-Y., & Teng, H. (2022). Melem-derived poly (heptazine imide) for effective charge transport and photocatalytic reforming of cellulose into H2 and biochemicals under visible light. Applied Catalysis B: Environmental, 316, 121601.
11. Guayaquil-Sosa, J. F., Serrano-Rosales, B., Valadés-Pelayo, P. J., & de Lasa, H. (2017). Photocatalytic hydrogen production using mesoporous TiO2 doped with Pt. Applied Catalysis B: Environmental, 211, 337-348.
12. Chen, Y., Lin, B., Wang, H., Yang, Y., Zhu, H., Yu, W., & Basset, J.-m. (2016). Surface modification of g-C3N4 by hydrazine: Simple way for noble-metal free hydrogen evolution catalysts. Chemical Engineering Journal, 286, 339-346.
13. Li, Z., Feng, H., Song, M., He, C., Zhuang, W., & Tian, L. (2021). Advances in CoP electrocatalysts for water splitting. Materials Today Energy, 20, 100698.
14. Ji, P., Luo, X., Chen, D., Jin, H., Pu, Z., Zeng, W., He, J., Bai, H., Liao, Y., & Mu, S. (2020). Significantly improved water oxidation of CoP catalysts by electrochemical activation. ACS Sustainable Chemistry & Engineering, 8(48), 17851-17859.
15. Luna, A. L., Dragoe, D., Wang, K., Beaunier, P., Kowalska, E., Ohtani, B., Bahena Uribe, D., Valenzuela, M. A., Remita, H., & Colbeau-Justin, C. (2017). Photocatalytic hydrogen evolution using Ni–Pd/TiO2: correlation of light absorption, charge-carrier dynamics, and quantum efficiency. The Journal of Physical Chemistry C, 121(26), 14302-14311.
16. Zeng, D., Wang, H., Zhu, X., Cao, H., Zhou, Y., Wang, W., Zhang, L., & Wang, W. (2023). Single-atom copper modified hexagonal tungsten oxide for efficient photocatalytic CO2 reduction to acetic acid. Chemical Engineering Journal, 451, 138801.

17. Albero, J., Peng, Y., & García, H. (2020). Photocatalytic CO2 reduction to C2+ products. Acs Catalysis, 10(10), 5734-5749.
18. Xu, W., Liu, Z., Johnston-Peck, A. C., Senanayake, S. D., Zhou, G., Stacchiola, D., Stach, E. A., & Rodriguez, J. A. (2013). Steam reforming of ethanol on Ni/CeO2: reaction pathway and interaction between Ni and the CeO2 support. Acs Catalysis, 3(5), 975-984.
19. de Lima, S. M., da Silva, A. M., da Costa, L. O., Assaf, J. M., Jacobs, G., Davis, B. H., Mattos, L. V., & Noronha, F. B. (2010). Evaluation of the performance of Ni/La2O3 catalyst prepared from LaNiO3 perovskite-type oxides for the production of hydrogen through steam reforming and oxidative steam reforming of ethanol. Applied Catalysis A: General, 377(1-2), 181-190.
20. Walenta, C. A., Courtois, C., Kollmannsberger, S. L., Eder, M., Tschurl, M., & Heiz, U. (2020). Surface species in photocatalytic methanol reforming on Pt/TiO2 (110): learning from surface science experiments for catalytically relevant conditions. Acs Catalysis, 10(7), 4080-4091.
21. Xiong, M., Qin, Y., Chai, B., Yan, J., Fan, G., Xu, F., Wang, C., & Song, G. (2022). Unveiling the role of Mn-Cd-S solid solution and MnS in MnxCd1-xS photocatalysts and decorating with CoP nanoplates for enhanced photocatalytic H2 evolution. Chemical Engineering Journal, 428, 131069.
22. Carter, D. B. W. C. B. (2009). Transmission electron microscopy A textbook for materials science.
23. Spence, J. C. (2013). High-resolution electron microscopy. OUP Oxford.
24. Jinschek, J. (2014). Advances in the environmental transmission electron microscope (ETEM) for nanoscale in situ studies of gas–solid interactions. Chemical Communications, 50(21), 2696-2706.
25. Wachs, I. E., & Bañares, M. A. (2023). Springer Handbook of Advanced Catalyst Characterization. Springer Nature.
26. Farrukh, M. A. (2012). Advanced aspects of spectroscopy. BoD–Books on Demand.

27. Mohamed, M. A., Jaafar, J., Ismail, A., Othman, M., & Rahman, M. (2017). Fourier transform infrared (FTIR) spectroscopy. In Membrane characterization (pp. 3-29). Elsevier.
28. Corcoran, C., Tavassol, H., Rigsby, M., Bagus, P., & Wieckowski, A. (2010). Application of XPS to study electrocatalysts for fuel cells. Journal of Power Sources, 195(24), 7856-7879.
29. Rocha, F. S., Gomes, A. J., Lunardi, C. N., Kaliaguine, S., & Patience, G. S. (2018). Experimental methods in chemical engineering: Ultraviolet visible spectroscopy—UV-Vis. The Canadian Journal of Chemical Engineering, 96(12), 2512-2517.
30. Guo, Y., Liu, C., Ye, R., & Duan, Q. (2020). Advances on water quality detection by uv-vis spectroscopy. Applied Sciences, 10(19), 6874.
31. Li, Q., Anpo, M., & Wang, X. (2020). Application of photoluminescence spectroscopy to elucidate photocatalytic reactions at the molecular level. Research on Chemical Intermediates, 46(10), 4325-4344.
32. Gfroerer, T. H. (2000). Photoluminescence in analysis of surfaces and interfaces. Encyclopedia of analytical chemistry, 67, 3810.
33. Olthof, S. (2021). The impact of UV photoelectron spectroscopy on the field of organic optoelectronics—a retrospective. Advanced Optical Materials, 9(14), 2100227.
34. Ghaffari, M., Shannon, M., Hui, H., Tan, O. K., & Irannejad, A. (2012). Preparation, surface state and band structure studies of SrTi (1− x) Fe (x) O (3− δ)(x= 0–1) perovskite-type nano structure by X-ray and ultraviolet photoelectron spectroscopy. Surface science, 606(5-6), 670-677.
35. Vivekanandan-Giri, A., Byun, J., & Pennathur, S. (2011). Quantitative analysis of amino acid oxidation markers by tandem mass spectrometry. In Methods in enzymology (Vol. 491, pp. 73-89). Elsevier.

36. Beltrán-Suito, R., Menezes, P. W., & Driess, M. (2019). Amorphous outperforms crystalline nanomaterials: surface modifications of molecularly derived CoP electro (pre) catalysts for efficient water-splitting. Journal of Materials Chemistry A, 7(26), 15749-15756.

37. Mei, P., Yamauchi, Y., Pramanik, M., Fatehmulla, A., Adhafiri, A. M., Farooq, W. A., Bando, Y., Shiddiky, M. J., Kaneti, Y. V., & Lin, J. (2019). Hard-templated preparation of mesoporous cobalt phosphide as an oxygen evolution electrocatalyst. Electrochemistry Communications, 104, 106476.

38. Chueh, L. C., Lin, T. J., Lee, H. C., & Wu, J. J. (2024). Defective Potassium Poly (Heptazine Imide) Preventing Spin Delocalization and Hole Transfer Deactivation for Efficient Solar Energy Conversion and Storage. Small, 20(5), 2304813.

39. Li, H., Zhang, G., Zhang, P., & Mi, H. (2024). In-situ one-step construction of poly (heptazine imide)/poly (triazine imide) heterojunctions for photocatalytic hydrogen evolution. ChemSusChem, e202301849.

40. Ma, L., Shen, X., Zhou, H., Zhu, G., Ji, Z., & Chen, K. (2015). CoP nanoparticles deposited on reduced graphene oxide sheets as an active electrocatalyst for the hydrogen evolution reaction. Journal of Materials Chemistry A, 3(10), 5337-5343.

41. Jiang, P., Liu, Q., Ge, C., Cui, W., Pu, Z., Asiri, A. M., & Sun, X. (2014). CoP nanostructures with different morphologies: synthesis, characterization and a study of their electrocatalytic performance toward the hydrogen evolution reaction. Journal of Materials Chemistry A, 2(35), 14634-14640.

42. Qi, K., Lv, W., Khan, I., & Liu, S.-y. (2020). Photocatalytic H2 generation via CoP quantum-dot-modified g-C3N4 synthesized by electroless plating. Chinese Journal of Catalysis, 41(1), 114-121.

43. Liu, Y., Zhang, J., Li, X., Yao, Z., Zhou, L., Sun, H., & Wang, S. (2019). Graphitic carbon nitride decorated with CoP nanocrystals for enhanced photocatalytic and photoelectrochemical H2 evolution. Energy & Fuels, 33(11), 11663-11676.

44. Chen, B., Lu, W., Xu, P., & Yao, K. (2023). Potassium poly (heptazine imide) coupled with Ti3C2 MXene-derived TiO2 as a composite photocatalyst for efficient pollutant degradation. ACS omega, 8(12), 11397-11405.
45. Wang, W., Shu, Z., Liao, Z., Zhou, J., Meng, D., Li, T., Zhao, Z., & Xu, L. (2021). Sustainable one-step synthesis of nanostructured potassium poly (heptazine imide) for highly boosted photocatalytic hydrogen evolution. Chemical Engineering Journal, 424, 130332.
46. Li, X., Chen, X., Fang, Y., Lin, W., Hou, Y., Anpo, M., Fu, X., & Wang, X. (2022). High-performance potassium poly (heptazine imide) films for photoelectrochemical water splitting. Chemical science, 13(25), 7541-7551.
47. Zhao, H., Jiang, P., & Cai, W. (2017). Graphitic C3N4 decorated with CoP co-catalyst: enhanced and stable photocatalytic H2 evolution activity from water under visible-light irradiation. Chemistry–An Asian Journal, 12(3), 361-365.
48. Yang, Z., Li, L., Gao, J., Zeng, S., Cui, J., Shao, S., Wang, K., Ma, D., Hu, C., & Zhao, Y. (2022). Optimizing the band structure of crystalline potassium poly (heptazine imide) for enhanced photocatalytic H2O2 production and pollutant degradation. ACS ES&T Engineering, 2(11), 2142-2149.
49. Thang, P. Q., Jitae, K., Nguyen, T. D., Huong, P. T., Viet, N. M., & Al Tahtamouni, T. (2019). Improvement of hydrogen production under solar light using cobalt (II) phosphide hydroxide co-doped gC 3 N 4 photocatalyst. Rendiconti Lincei. Scienze Fisiche e Naturali, 30, 699-706.
50. Lin, L., Ou, H., Zhang, Y., & Wang, X. (2016). Tri-s-triazine-based crystalline graphitic carbon nitrides for highly efficient hydrogen evolution photocatalysis. Acs Catalysis, 6(6), 3921-3931.
51. Yao, Y., Li, Q., Dai, X., Dai, P., & Xu, D. (2022). A novel hierarchical CdS-DETA@ CoP composite as highly stable photocatalyst for efficient H2 evolution from water splitting under visible light irradiation. Applied Surface Science, 588, 152890.

52. Liu, Y., Zhu, Y., Shen, J., Huang, J., Yang, X., & Li, C. (2018). CoP nanoparticles anchored on N, P-dual-doped graphene-like carbon as a catalyst for water splitting in non-acidic media. Nanoscale, 10(5), 2603-2612.
53. Zhao, D., Sun, B., Li, X., Qin, L., Kang, S., & Wang, D. (2016). Promoting visible light-driven hydrogen evolution over CdS nanorods using earth-abundant CoP as a cocatalyst. RSC advances, 6(39), 33120-33125.
54. Zong, S., Tian, L., Guan, X., Cheng, C., Shi, J., & Guo, L. (2022). Photocatalytic overall water splitting without noble-metal: Decorating CoP on Al-doped SrTiO3. Journal of Colloid and Interface Science, 606, 491-499.
55. Wang, F., Li, J., Yu, X., Tang, H., Xu, J., Sun, L., & Liu, Q. (2023). Unveiling the role of metallic CoP@ Ni2P sea-urchin-like nanojunction as a photothermal cocatalyst for enhancing the H2 generation and benzaldehyde formation over CdZnS nanoparticles. Journal of Materials Science & Technology, 146, 49-60.
56. Hao, X., Shao, Y., Xiang, D., & Jin, Z. (2022). Photocatalytic overall water splitting hydrogen production over ZnCdS by spatially-separated WP and Co3O4 cocatalysts. Solar Energy Materials and Solar Cells, 248, 111970.
57. Yang, J., Wang, D., Han, H., & Li, C. (2013). Roles of cocatalysts in photocatalysis and photoelectrocatalysis. Accounts of chemical research, 46(8), 1900-1909.
58. Nguyen, V.-C., Sanoe, M., Putri, N. P., Lee, Y.-L., & Teng, H. (2024). Co-catalyst design to control charge transfer and product composition for photocatalytic H 2 production and biomass reforming. Sustainable Energy & Fuels, 8(7), 1412-1423.
59. Nguyen, V.-C., Nimbalkar, D. B., Huong, V. H., Lee, Y.-L., & Teng, H. (2023). Elucidating the mechanism of photocatalytic reduction of bicarbonate (aqueous CO2) into formate and other organics. Journal of Colloid and Interface Science, 649, 918-928.
60. Makino, K., Mossoba, M. M., & Riesz, P. (1982). Chemical effects of ultrasound on aqueous solutions. Evidence for hydroxyl and hydrogen free radicals (. cntdot. OH and. cntdot. H) by spin trapping. Journal of the American Chemical Society, 104(12), 3537-3539.

61. DuBose, C., Rehorek, D., Oehler, U., & Janzen, E. (1988). Spin trapping: ESR parameters of spin adducts. Free Radical Biology & Medicine, 5(1), 55-56.
62. Yan, W., Li, N., Yan, Z., & Wang, Z. (2023). Photo-Fenton-induced selective dehydrogenative coupling of methanol into ethylene glycol over iron species-anchored TiO 2 nanorods. Catalysis Science & Technology, 13(5), 1482-1487.
63. Ma, J., Mao, K., Low, J., Wang, Z., Xi, D., Zhang, W., Ju, H., Qi, Z., Long, R., & Wu, X. (2021). Efficient photoelectrochemical conversion of methane into ethylene glycol by WO3 nanobar arrays. Angewandte Chemie, 133(17), 9443-9447.
64. Zhang, H., Xie, S., Hu, J., Wu, X., Zhang, Q., Cheng, J., & Wang, Y. (2020). C–H activations of methanol and ethanol and C–C couplings into diols by zinc–indium–sulfide under visible light. Chemical Communications, 56(12), 1776-1779.
65. Putri, N. P., Nguyen, V.-C., Sanoe, M., Lee, Y.-L., & Teng, H. (2024). Concurrent photocatalytic bicarbonate (aqueous-CO2) reduction and xylose reforming to produce compounds from C—C coupling. Chemical Engineering Journal, 486, 150318.
66. Xiao, N., Li, S., Li, X., Ge, L., Gao, Y., & Li, N. (2020). The roles and mechanism of cocatalysts in photocatalytic water splitting to produce hydrogen. Chinese Journal of Catalysis, 41(4), 642-671.
67. Pan, Z., Zheng, Y., Guo, F., Niu, P., & Wang, X. (2017). Decorating CoP and Pt nanoparticles on graphitic carbon nitride nanosheets to promote overall water splitting by conjugated polymers. ChemSusChem, 10(1), 87-90.
68. Singh, S., Kumar, V., Chauhan, A., Datta, S., Wani, A. B., Singh, N., & Singh, J. (2018). Toxicity, degradation and analysis of the herbicide atrazine. Environmental chemistry letters, 16, 211-237.
69. Parra, S., Stanca, S. E., Guasaquillo, I., & Thampi, K. R. (2004). Photocatalytic degradation of atrazine using suspended and supported TiO2. Applied Catalysis B: Environmental, 51(2), 107-116.

70. Tolosana-Moranchel, A., Pecharromán, C., Faraldos, M., & Bahamonde, A. (2021). Strong effect of light scattering by distribution of TiO2 particle aggregates on photocatalytic efficiency in aqueous suspensions. Chemical Engineering Journal, 403, 126186.
71. Chiarello, G. L., Aguirre, M. H., & Selli, E. (2010). Hydrogen production by photocatalytic steam reforming of methanol on noble metal-modified TiO2. Journal of Catalysis, 273(2), 182-190.
72. Zhang, R., Ye, M., Yang, Y. N., Huang, R., Wang, X. L., & Yao, Y.-F. (2020). Operando NMR study on the effect of photon flux and wavelength on photocatalytic reforming of methanol. Journal of Catalysis, 382, 173-180.
73. Yu, F., Chen, L., Li, X., Shen, X., Zhao, H., Duan, C., & Chen, Q. (2021). Cu nanocluster-loaded TiO2 nanosheets for highly efficient generation of CO-free hydrogen by selective photocatalytic dehydrogenation of methanol to formaldehyde. ACS Applied Materials & Interfaces, 13(16), 18619-18626.
74. Huang, H., Jin, Y., Chai, Z., Gu, X., Liang, Y., Li, Q., Liu, H., Jiang, H., & Xu, D. (2019). Surface charge-induced activation of Ni-loaded CdS for efficient and robust photocatalytic dehydrogenation of methanol. Applied Catalysis B: Environmental, 257, 117869.
75. Tasleem, S., & Tahir, M. (2021). Constructing La x Co y O3 Perovskite Anchored 3D g-C3N4 Hollow Tube Heterojunction with Proficient Interface Charge Separation for Stimulating Photocatalytic H2 Production. Energy & Fuels, 35(11), 9727-9746.
76. Li, Z., Ivanenko, A., Meng, X., & Zhang, Z. (2019). Photocatalytic oxidation of methanol to formaldehyde on bismuth-based semiconductors. Journal of hazardous materials, 380, 120822.
77. Xu, B.-B., Zhou, M., Zhang, R., Ye, M., Yang, L.-Y., Huang, R., Wang, H. F., Wang, X. L., & Yao, Y.-F. (2020). Solvent water controls photocatalytic methanol reforming. The Journal of Physical Chemistry Letters, 11(9), 3738-3744.

78. Xu, B.-B., Zhou, M., Ye, M., Yang, L.-Y., Wang, H.-F., Wang, X. L., & Yao, Y.-F. (2021). Cooperative Motion in Water–Methanol Clusters Controls the Reaction Rates of Heterogeneous Photocatalytic Reactions. Journal of the American Chemical Society, 143(29), 10940-10947.
79. Fontelles-Carceller, O., Muñoz-Batista, M. J., Conesa, J. C., Kubacka, A., & Fernández-García, M. (2018). H2 photo-production from methanol, ethanol and 2-propanol: Pt-(Nb) TiO2 performance under UV and visible light. Molecular Catalysis, 446, 88-97.
80. Zhang, S., Gong, X., Shi, Q., Ping, G., Xu, H., Waleed, A., & Li, G. (2020). CuO nanoparticle-decorated TiO2-nanotube heterojunctions for direct synthesis of methyl formate via photo-oxidation of methanol. ACS omega, 5(26), 15942-15948.
81. Liu, J., Han, C., Yang, X., Gao, G., Shi, Q., Tong, M., Liang, X., & Li, C. (2016). Methyl formate synthesis from methanol on titania supported copper catalyst under UV irradiation at ambient condition: Performance and mechanism. Journal of Catalysis, 333, 162-170.
82. Xie, S., Shen, Z., Deng, J., Guo, P., Zhang, Q., Zhang, H., Ma, C., Jiang, Z., Cheng, J., & Deng, D. (2018). Visible light-driven C− H activation and C–C coupling of methanol into ethylene glycol. Nature Communications, 9(1), 1-7.
83. Uddin, N., Langley, J., Zhang, C., Fung, A. K., Lu, H., Yin, X., Liu, J., Wan, Z., Nguyen, H. T., & Li, Y. (2021). Zero-emission multivalorization of light alcohols with self-separable pure H2 fuel. Applied Catalysis B: Environmental, 292, 120212.
84. Uddin, N., Langley, J., Zhang, C., Fung, A. K., Lu, H., Yin, X., Liu, J., Wan, Z., Nguyen, H. T., & Li, Y. (2021). Zero-emission multivalorization of light alcohols with self-separable pure H2 fuel. Applied Catalysis B: Environmental, 292, 120212.

85. Chang, A., Peng, W.-S., Tsai, I.-T., Chiang, L.-F., & Yang, C.-M. (2019). Efficient hydrogen production by selective alcohol photoreforming on plasmonic photocatalyst comprising sandwiched Au nanodisks and TiO2. Applied Catalysis B: Environmental, 255, 117773.